RSC Applied Interfaces

Accepted Manuscript

This article can be cited before page numbers have been issued, to do this please use: S. S. M. Bhat and S. G. Kumar, *RSC Appl. Interfaces*, 2025, DOI: 10.1039/D5LF00154D.

ROYAL SOCIETY OF CHEMISTRY

rsc.li/RSCApplInter

View Article Online
DOI: 10.1039/D5LF00154D

Recent advances in interface engineering of bismuth-based materials for photocatalytic CO_2 reduction

Swetha S. M. Bhat[a]* and Girish Kumar S.[a]

[a]Department of Chemistry, RV College of Engineering, Mysuru Road, Bengaluru-560059, India. E-mail: swethasm@rvce.edu.in

Abstract

Photocatalytic reduction of CO_2 into value added products is witnessed as a promising technology to mitigate both global warming and energy crisis. Among the illustrious functional semiconductors, bismuth-based materials are feasible for the CO_2 reduction reaction owing to their convenient preparation, narrow band gap and the availability of hybridized energy states in the conduction band. Furthermore, the inherent 2D layered structure of few Bi-materials remains as an added advantage for various photocatalytic reactions. In this focused review, interfacial engineering of Bi-based semiconductors achieved by coupling them with distinct photocatalytic materials to form Type-I, Type-II, Z-scheme or S-scheme heterojunction are discussed and their application towards CO_2 reduction reactions are emphasized. The further advancements including the co-catalyst loading, defect engineering and designing with hierarchical morphology from the prospect of improving the charge carrier separation and structural stability are highlighted. The preparation methods and the mechanistic pathways for the CO_2 reduction reaction are briefly summarized at the relevant places. Finally, the challenges and scope of Bi-based materials to spotlight their applications in energy-environmental related areas are presented.

View Article Online
DOI: 10.1039/D5LF00154D

1.0 Introduction

Global energy consumption has skyrocketed in recent decade using nonrenewable fossil fuels, leading to significant global climate changes and imbalance in the ecosystem. As per the literature, CO_2 emission has substantially increased by ~40 % since the industrial revolution.[1, 2] Therefore, the development of efficient method to convert CO_2 to value added products have drawn the attention as they can conveniently address the environmental issues and the energy demands.[3] Numerous technologies such as chemical reforming, biological, electrochemical, photocatalytic, and photoelectrocatalytic processes are extensively investigated over the years to address these issues.[4-9] Among them, photocatalytic CO_2 reduction is found to be a sustainable solution for the removal of atmospheric CO_2 and transform them to selective gaseous (methane, ethane) and liquid phase products (formate, methanol, ethanol).[10-12] Compared to other approaches, this technique benefits from superior product selectivity, economic viability and environmentally benign.[13] The linear CO_2 with sp^2 hybridization in C=O bonds require more dissociation energy compared to C-C and C-H bond and adequate amount of energy is required to activate CO_2 molecules.[14, 15] The primary step in the reduction process demands the strong adsorption of CO_2 on the catalytic surface, which is subsequently followed by its activation by the surface active sites.[16-18] The CO_2 photoreduction imitates the photosynthesis of plants where it utilizes water and CO_2 and convert them into chemical fuels such as methane, methanol and value added multi carbon products. The reaction product ratio will vary with number of electrons participating in the reaction, nature of photocatalytic materials and the adopted reaction conditions.[14-18]

The primary step in the semiconductor photocatalysis involves the absorption of light energy by the catalysts greater than or equal to its band gap to generate electron-hole pairs. These excitons migrate towards the surface and interacts with the adsorbed species to produce the products *via* redox reactions, which later desorb from the surface of the catalyst.[19] As per

View Article Online
DOI: 10.1039/D5LF00154D

theoretical calculations and kinetic studies, it is reported that the CO, COOH and COH are common intermediates for CO_2 reduction reaction.[20] The CO_2 photoreduction will proceed only when the energy of the conduction band of the concerned semiconductor is more negative than the reduction potential of the desired products.[2] Semiconductors such as BiOX, CdS, g-C_3N_4, Cu_2O, SnO_2, TiO_2, ZnO, and perovskites are extensively used for CO_2 reduction reaction.[21-31] The bismuth-based materials has garnered major interests as they possess band gap spanning the major portion of the solar spectrum and band edge positions are convenient to trigger desired reduction and oxidation reactions.[32-37] The Bi 6*s* orbital hybridize with O 2*s* orbital to form highly dispersive energy band structure which promotes charge carrier transport and also exhibits high oxidizing capabilities. Furthermore, bismuth based materials offer stable structure with layered spaces to promote the intercalation of foreign ions without changing their structural features. Being less toxic, environmentally friendly and remarkably photostable, the distinct morphology of bismuth-based materials have been explored for photocatalytic applications.[11, 38] Different categories of bismuth based materials such as unitary (Bi), binary (Bi_2S_3, Bi_2O_3), and ternary (stoichiometric and non-stochiometric bismuth oxy halides, $BiVO_4$, Bi_2WO_6, Bi_2MoO_6) are used for photocatalytic CO_2 reduction.[36, 39-41] However, massive charge carrier recombination and narrow optical response of single phase photocatalysts limits their performance under the light illuminated conditions.[39, 42, 43] Several reviews on bismuth-based materials towards photocatalytic applications can be found in the literature.[37, 38, 41, 44, 45] However, recent trend in the interfacial engineering of these materials is scarcely emphasized. Motivated by these aspects, this review summarizes the interfacial engineering of bismuth-based materials with various semiconductors under different reaction conditions and their performance towards photocatalytic CO_2 reduction are outlined.

View Article Online
DOI: 10.1039/D5LF00154D

2.0 Strategies for interfacial engineering

Heterojunction of semiconductors found to be a promising method to improve the photocatalytic performance owing to the synergistic interactions arising from the structure-optical-morphological properties of the integrated semiconductors.[46-49] The prime requisite to fabricate a heterojunction is that the band position of the concerned semiconductors must possess different potentials to achieve maximum separation of the charge carriers.[50, 51] Secondly, the bandgap response of the individual components must be substantially different so that the composite absorbs larger fraction of the solar light for the photocatalytic reactions. The various types of heterojunctions have been fabricated for bismuth-based materials to increase the conversion efficiency of CO_2 to value added products. Following are the methods that have been adopted extensively for various types of bismuth-based materials:

(i) Type-II heterojunction: When two semiconductors with different band edge potentials and Fermi levels encounters each other, three types of heterojunctions such as Type-I, Type-II and Type-III are formed. The Type-I allows for the migration of both the charge carriers from one semiconductor to another owing to their straddle bandgap configuration, which enhances the charge carrier recombination (Figure 1). In contrast, Type-II is efficient in separating the electron-hole pairs due to the staggered configuration of the electronic band positions. It is also referred to as cascade electron transfer process, as it promotes interfacial charge carrier separation. However, the potential of electrons and holes decreases lowering the efficiency of the composite.

(ii) Z-scheme: Though type II heterojunction can improve the photocatalytic activity, they suffer from recombination of electron and holes. This disadvantage can be avoided by Z-scheme technique.[52]

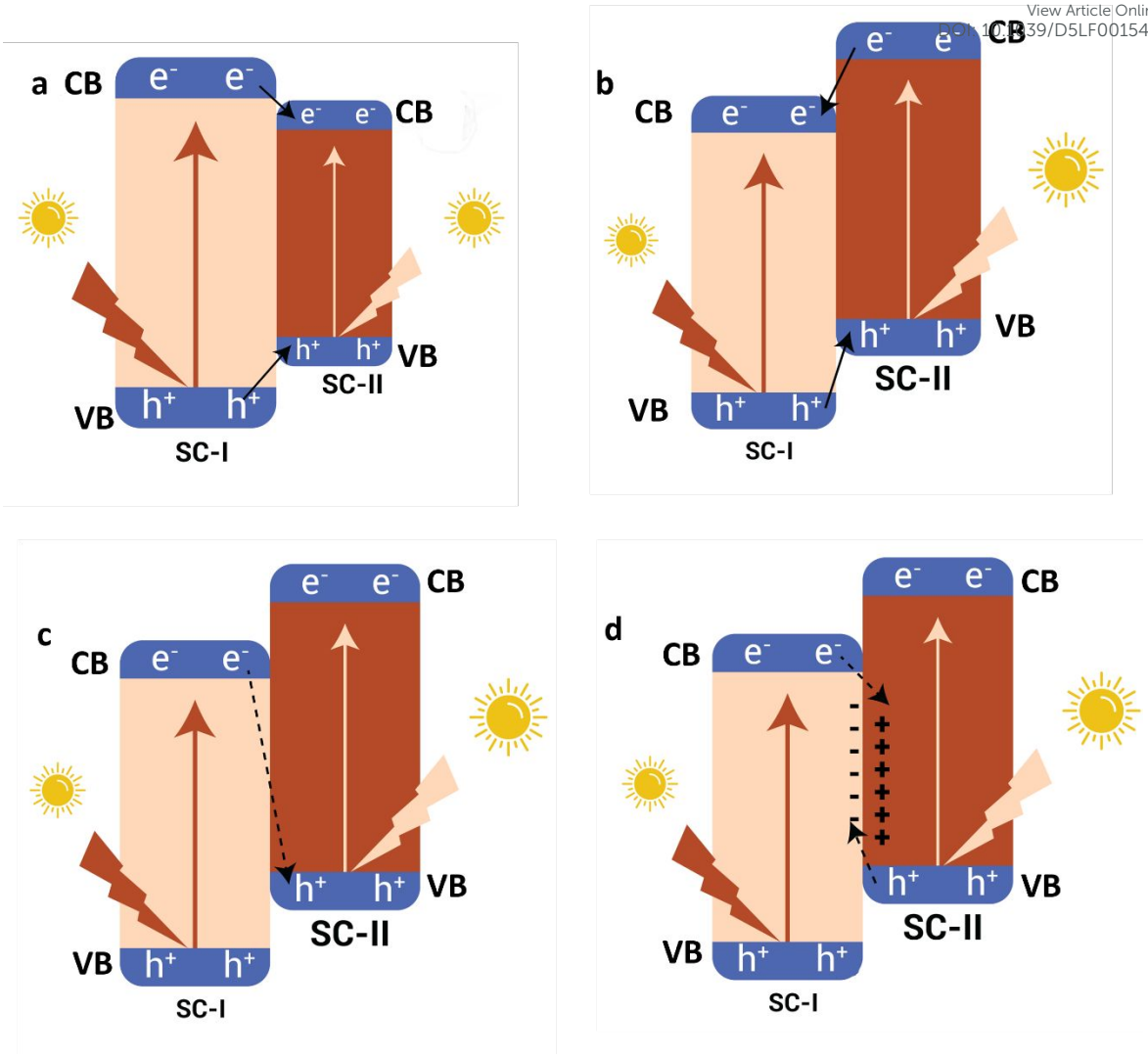

Figure 1. Different types of semiconductor-semiconductor heterojunction: a) Type-I, b) Type-II, c) Z-scheme, and d) S-scheme heterojunction. Note: SC = semiconductors; CB = conduction band; VB = valence band.

Band gap configuration in Z-scheme is similar to Type-II configuration, but an exception remains in the direction of electron transfer pathways. The less potential electrons accumulated on one side of the semiconductor recombine with less potential holes of another semiconductor, thereby retaining the high potential electrons and holes for the redox reactions.

View Article Online
DOI: 10.1039/D5LF00154D

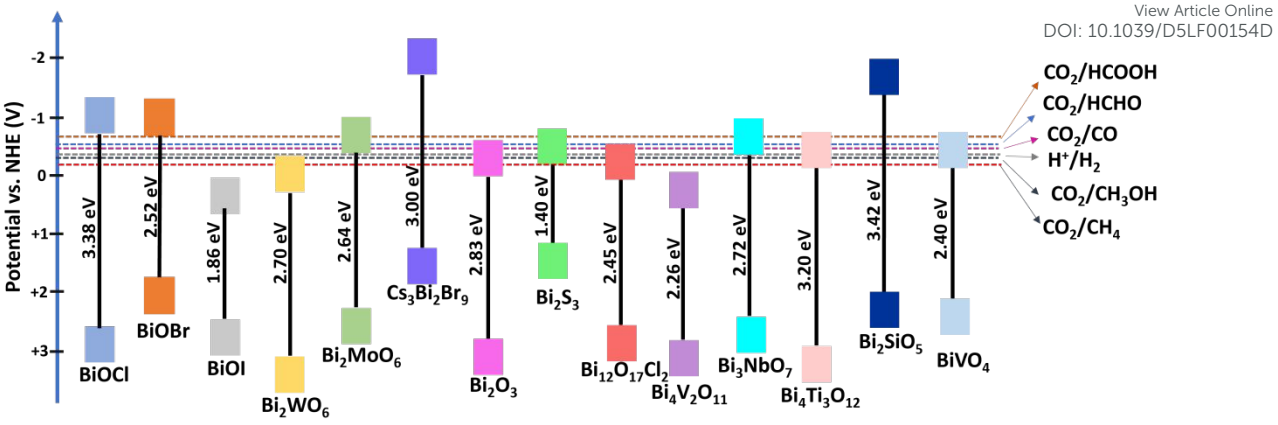

Figure 2. Band positions of different bismuth based semiconductors.

Though, significant improvement can be observed from Z-scheme photocatalysis, this technique also fails to deliver superior photocatalytic performance as the limitation arises from the choice of the semiconductors.[53]

(iii) S-Scheme heterojunction: Step scheme (S-scheme) was introduced by Jiaguo Yu group.[54, 55] When reduction and oxidation photocatalysts are in close contact, the electrons in the oxidation photocatalyst recombines with holes present in the valence band of the reduction photocatalyst. The positive and negative charge is formed at reduction and oxidation photocatalyst and the direction of in-built electric field emerges from reduction to oxidation photocatalyst. Thus, the electron depletion at the reduction photocatalyst causes the upward band bending and electron accumulation at the oxidation photocatalyst results in the downward band bending. Driven by the rise of electric field and the Coulombic force of attraction, the electrons in oxidation photocatalyst recombine with holes in the reduction photocatalyst, while preserving the energetic charge carriers for the desired redox reactions.[55] The preserved electrons and holes are available for reaction to take place making the photocatalytic system to be more efficient than Type-II and Z-scheme heterojunction. The position of conduction and valence band for different bismuth based materials clearly signifies their ability to participate in the CO_2 reduction reactions (Figure 2).

View Article Online
DOI: 10.1039/D5LF00154D

(iv) Cocatalyst loading

The cocatalysts such as noble metals which include Pt, Ag and Au, non-noble metals such as Bi, Cu, and Mg have been exploited to improve the performance of the photocatalytic process.[56-58] The activation energy required to convert CO_2 to any value-added products can be reduced with the addition of cocatalysts on the semiconductor surface. It is also found from the literature that the it increases the reaction site and play a vital role in determining the selectivity, adsorption of CO_2, and photostability of the photocatalyst.[59, 60]

(v) Defect engineering: Defects are of paramount importance in tailoring the bandgap and charge carrier dynamics of functional semiconductors. In general, anionic vacancies like oxygen vacancies can narrow the gap region and shift the optical response of the host matrix to the visible region. Few reports also hints that the tailoring the bandgap depending on the density of oxygen vacancies in the host matrix.[61, 62] Furthermore, oxygen vacancies can also trap the charge carriers to restrain their recombination with holes and extends the charge carrier lifetime. On the other hand, cationic vacancies can temporarily trap the holes. In recent times, vacancy engineering for Bi-based materials is reported to show superior photocatalytic activity compared to less defective counterparts.[45, 63, 64] These defects can alter the lattice strain and surface defects which can facilitate the adsorption of oxygen, to promote the formation of superoxide radicals in the solution phase.[65]

3.0 Bi-based semiconductors

3.1 BiOX

BiOX is highly crystalline with tetragonal crystal structure and extensively used for photocatalytic applications due to its layered structure and narrow band gap.[66] It is composed of layered structure with $[Bi_2O_2]$ slabs and two arrays of $[X]^-$ ions. The exciton pairs can be effectively separated as the charge density is higher in Bi-O than that of [X] slabs. In addition,

View Article Online
DOI: 10.1039/D5LF00154D

static electric field along the *c*-axis avoids the massive charge carrier recombination pathways.[67] The BiOCl is an indirect band gap semiconductor which decreases the chance of recombination of the charge carriers.[68-71] Defects in BiOX can influence the photocatalytic activity by modifying charge transport and electronic structure of the material. The oxygen vacancy can be introduced easily to the BiOCl as Bi-O bond is weak. These oxygen vacancy can increase the number of active sites to facilitate the CO_2 adsorption and activation process.[72] It has been observed that the majority of BiOX based heterojunctions produce only CO and CH_4 and therefore, interfacial engineering of BiOX plays a crucial role in improving the selectivity.[73] The crystal facet of BiOCl also influence the photocatalytic activity when coupled with CdS. The CdS/BiOCl with exposed facet exhibited higher performance compared to facets.[67] This was attributed to the effective coupling of interfacial electric field of the heterojunction and the polarization electric field of {001} crystal facet of BiOCl. The CH_4 and CO production with {001} -BiOCl/CdS was higher compared to the (zero one zero)-BiOCl/CdS, despite the bandgap energy and band edge potential of both the facets were almost similar. This result suggests that the crystal facet orientation of BiOCl has profound influence on the adsorption and activation of CO_2. As the polarization electric field for BiOCl is along the *c*-axis, excited electrons easily accumulate on the {001} facet, which favour their recombination with valence band holes of CdS, thereby improving the energetic electrons and holes from CdS and BiOCl respectively to participate in the redox reactions.[67] The 2D/2D Vo-WO_x/BiOCl S-scheme has been fabricated by a self-assembly process. S-scheme heterojunction not only offered separation of photogenerated charge carriers but also provided dual interfacial pathway to improve the charge separation process.[74] Jiang *et al*. showed that the CO_2 molecules adsorbed on BiOCl (001) and WOx (010) surface.[75] The study also suggested that CO_2 molecules are more stable on BiOCl surface than that of WO_x. The conduction band level for WO_x is not sufficient to carry out reduction of CO_2 molecules. As a

View Article Online
DOI: 10.1039/D5LF00154D

result, the adsorption and reaction sites are available only on the surface of BiOCl.[75] Similarly, Bi_2WO_6 has also been used to fabricate the heterojunction with BiOCl. Unlike S-scheme as in WO_x/BiOCl, they formed typical Type-II heterojunction. Theoretical calculations confirm that the production of CHO* intermediate on the surface of BiOCl/Bi_2WO_6 is responsible for the selective generation of CH_4. The high selectivity towards CH_4 is due to ultrathin nanosheet morphology (2D/2D) and the presence of internal electric field at the heterointerface.[76] BiOCl/In_2O_3 fabricated by hydrothermal method with Type-II heterojunction yielded with high rate of CO_2 photoreduction.[77] Enhanced performance was attributed to the narrow band gap which falls in the visible region. In another report, Chlorophyl and Mg co-modified BiOCl (Chl-Mg/BiOCl) microsphere exhibits superior photocatalytic applications. Chl-Mg/BiOCl yielded 100 μmol g^{-1} of CH_4. Chlorophyl on the surface of the BiOCl produces singlet states of Chl-Mg* which acts as an electron donor. Mg forms a complex with chlorophyl and helps in improving the stability of the catalyst.[78]

It is also noted that cocatalyst loading on the photocatalyst is a potential approach to improve the adsorption of the intermediates in CO_2 reduction there by influencing the coupling of C-C bond. To improve C_2 hydrocarbon selectivity and to enhance photocatalytic reduction of CO_2 transition metal cocatalyst with nanostructures have been loaded on BiOCl. [71, 79, 80] Selectivity towards CH_4 was increased by decorating with noble metal such as Pd on BiOCl. Pd has not only decreased the recombination of the charge carriers but also changed the intermediate formed (from HCO_3^- to HCOO* and CH_3O*, CH_3O* will be reduced to CH_4) on the surface of BiOCl.[80]

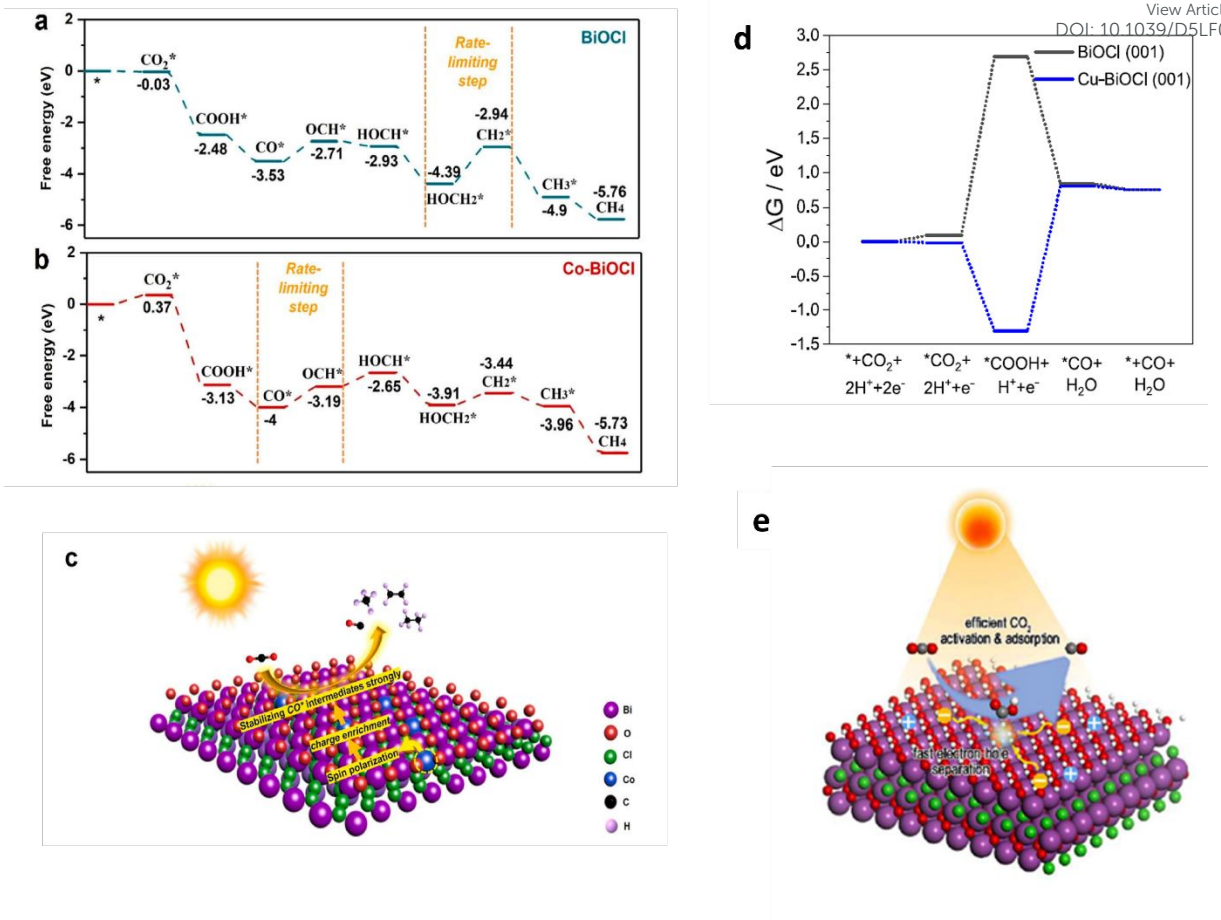

Figure 3. Computed Gibb's free energy main reactions for photocatalytic reduction of CO_2 on a) pristine BiOCl b) Co-BiOCl [79] d) Gibb's free energy diagram for CO_2 reduction in Cu-BiOCl e) scheme for photoreduction of CO_2 to CO. Reproduced with permission from ref. 68. Copyright 2022, American Chemical Society and ref. 79. Copyright 2024, Elsevier.

In situ diffused reflectance infrared Fourier transformation (DRIFT) revealed that the key intermediates are bidentate formate and methoxy which promotes the selectivity for CH_4 production.[80] Photocatalytic activity of BiOCl ultrathin sheets can be altered by introducing magnetically active metal particles. In this context, Li *et al.* reported that Co doped BiOCl selectively converts CO_2 to CH_4 and C_{2+} products which was not possible with the pristine BiOCl. The increase in the photocatalytic activity was due to Co-O bond on the Co-BiOCl.[79] The increased CO_2 adsorption is primarily responsible for the enhanced CO_2 photoreduction. It is also found that the introduction of Co on BiOCl generates spin polarized charge and

View Article Online
DOI: 10.1039/D5LF00154D

changes the intermediate formed on the surface of BiOCl. In order to generate CH_4 and C_{2+} products, CO* intermediate will be formed via the formation of COOH* intermediate (Figure 3a-c). The rate limiting step for Co-BiOCl is the conversion of CO* to CHO* whereas for BiOCl $HOCH_2$* to CH_2* was the rate limiting step.[79] This work shows that the spin polarization of the charge on the surface of BiOCl has resulted in the formation of stable intermediate and promoted C-C coupling to yield CH_4 and C_{2+} products. Similarly, Cu was modified on BiOCl nanosheets which resulted in surface charge distribution. Cu-BiOCl has improved the catalytic performance and enhanced the absorption of light.[71] Also, it has decreased the activation energy barrier, which facilitates the faster consumption of CO_2 molecules resulting in increased CO yield (Figure 3d-e). Metal cotalysts such as Pt, Pd and Au metals have been decorated on BiOCl nanostructures by deposition-precipitation method. The main product obtained with BiOCl is CO, while CH_4 production dominated after loading the metal cocatalyst.[81]

Chen *et al.* demonstrated that Z-scheme In_2S_3/BiOCl can be prepared by solution combustion synthesis. The nanopetals of BiOCl were decorated on the nanoflowers of In_2S_3 in solution combustion synthesis. In_2S_3/BiOCl nanostructures are evenly deposited on the surface of the nanowires of MnO_2.[82] Initially, In_2S_3 nanoflowers was synthesized by hydrothermal approach. The synthesized In_2S_3 nanoflowers were dissolved in thiourea and the bismuth nitrate precursor along with concentrated nitric acid stirred vigorously. To this solution urea and ammonium chloride was added and stirred constantly for 24 h. The In_2S_3/MnO_2/BiOCl was fabricated by using the suspension of In_2S_3/BiOCl by hydrothermal approach. Despite having higher solubility than In_2S_3, BiOCl grows on the surface of the In_2S_3.[82] In_2S_3/BiOCl deposits uniformly on MnO_2 nanowires which forms an assembly of hierarchical structures. It is noted from this work that the S^{2-} ions play a significant role in controlling the nucleation of In_2S_3, forming the morphology and controlling the size of the nanostructure. This ternary heterojunction exhibited photocatalytic reduction rate of CO_2 to CO (51.2 μmol $g^{-1}h^{-1}$), C_2H_4 (63.2 μmol $g^{-1}h^{-1}$), and CH_4

View Article Online
DOI: 10.1039/D5LF00154D

(42.4 μmol $g^{-1}h^{-1}$).[82] The observed synergistic effect is attributed to the Mn 3*d* electrons which has narrowed the band gap. The key intermediates of the photocatalytic reduction were CHO* and COOH* for the production of CO, CH_4 and C_2H_4.[83] BiOCl with BiOBr heterojunction was fabricated by mechanical method which yielded Type-I heterojunction.[84] This heterojunction reduced CO_2 to CO with the formation rate of 7.353 μmol$g^{-1}h^{-1}$.

$CsPbBr_3$ perovskite is attracting increased attention due to its visible light harvesting capability and its high conduction band position enhances the reduction capability.[85] Various heterojunctions have been constructed based on $CsPbBr_3$ perovskite as the pristine material suffers from severe recombination of charge carriers. A 2D/2D S-scheme heterojunction comprising BiOCl and $CsPbBr_3$ was fabricated by an efficient self-assembly method. The zeta potential measurements revealed the negative and positive surface charge density on BiOCl and $CsPbBr_3$ which can adhere to each other through electrostatic force of attraction. The nanosheets of perovskite were assembled on the nanosheets of BiOCl which provides face-to-face contact and strong interfacial area existed between them. This heterojunction gave much improved photocatalytic activity towards CO_2 reduction to form CO as major product and CH_4 as minor product.[85] The high content of $CsPbBr_3$ in the composite reduced the CO production, while the yield of CH_4 remained almost same irrespective of its content.[85]

Chen *et al*. synthesized BiOCl by hydrothermal method and the oxygen vacancy was introduced by heating at 60 ℃ in the vacuum oven.[86] The Z- scheme heterostructure was fabricated by vigorously stirring powders of BiOCl with oxygen vacancy and 2D g-C_3N_4 nanosheets in ultrasonic bath. It is found that the heterojunction can be constructed effectively, if the two individual components are stirred in the ultrasonic bath rather than on the magnetic stirrer.[86] Authors have observed that photocatalytic reduction of CO_2 to CO for interfacial oxygen vacancy induced g-C_3N_4/BiOCl heterostructure was 1.6 times more than the pristine g-C_3N_4/BiOCl.

View Article Online
DOI: 10.1039/D5LF00154D

Ternary composites of BiOCl with dual Z- scheme of BiOCl/g-C_3N_4/Ag_2CrO_4 has also been synthesized and found to give CO and CH_4 with yields of 30.20 and 81.21 μmol g^{-1} respectively.[87] It is possible to make ternary heterojunction with C_3N_4 and BiOCl using Ag_2CrO_4 photocatalyst. The dual Z-scheme heterojunction photocatalyst was synthesized by simple method. BiOCl/C_3N_4 was prepared by taking the Bi, C and N precursors and heating solvothermally using ethylene glycol as solvent for 12 h at 140 °C. However, The BiOCl/C_3N_4 /Ag_2CrO_4 was synthesized by stirring the powders of BiOCl/C_3N_4 and precursors of Ag^+ and Cr^{6+} ions for 2 h. When the ternary heterojunction is formed, the morphology of BiOCl, C_3N_4 and Ag_2CrO_4 was retained. The irregular shapes of Ag_2CrO_4 were uniformly decorated on the microspheres of BiOCl and nanosheets of C_3N_4. It is observed that the C_3N_4 provides charge transfer pathway to form dual Z-scheme heterojunctions.

$MgIn_2S_4$ is another chalcogenide, which exhibits promising band gap and photostability which is extensively used for removal of liquid pollutant and for the production of hydrogen.[88] Zhang *et al.* fabricated the S-scheme heterojunction of Bi-BiOCl/$MgIn_2S_4$ by hydrothermal technique and $NaBH_4$ reduction technique.[89] The microspheres of BiOCl with average diameter of 1 μm was obtained from hydrothermal method and Bi self-doped BiOCl was synthesized by treating BiOCl micorspheres with $NaBH_4$ followed by vacuum drying. Bi-BiOCl/$MgIn_2S_4$ was synthesized by *in situ* hydrothermal method and the obtained product exhibited ultrathin sheets of BiOCl dispersed on the surface of $MgIn_2S_4$ marigold flower. It is noted that $NaBH_4$ which is used as a reducing agent has influenced the morphology of BiOCl and caused the rough surfaces and loose internal structures.[89] The formed S-scheme heterojunction exhibited the conversion of CO_2 to CH_4 with the yield of 25.72 μmol/g.

View Article Online
DOI: 10.1039/D5LF00154D

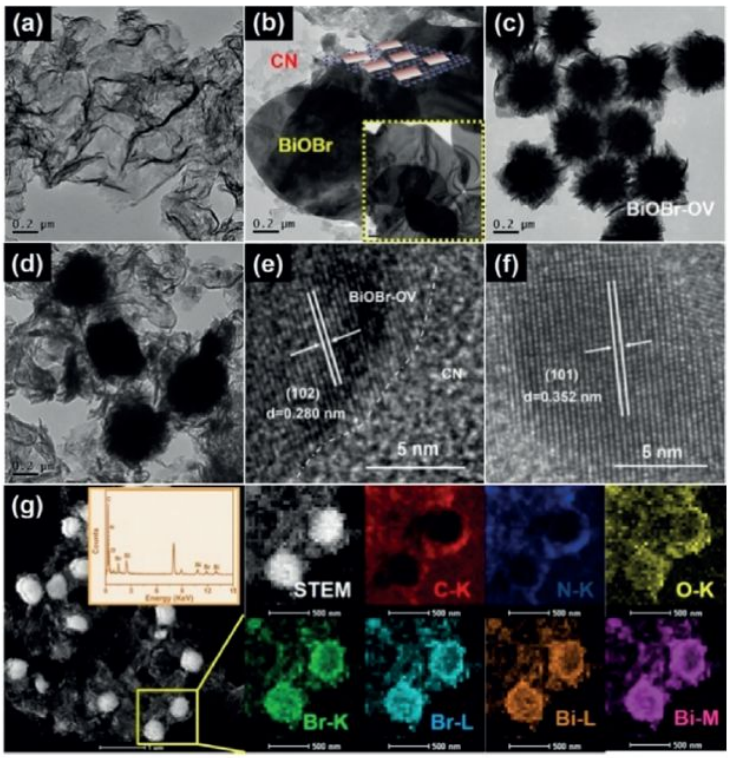

Figure 4. Transmission electron microscope (TEM) images of a) pure C_3N_4 (CN), b) CN-BiOBr, and BiOBr marked in the lower right corner, c) bare BiOBr-OV, d) CN-BiOBr-OV catalyst, e), f) High resolution (HR)-TEM images of CN-BiOBr-O_V heterojunction with the lattice spacings, and g) elemental maps of C, N, O, Br, and Bi in the CN BiOBr- O_V photocatalyst. Reproduced with permission from ref.91. Copyright 2020, Wiley-VCH.

BiOBr exhibits appropriate band structure, making it suitable for photocatalytic applications. However, the performance of BiOBr needs modification in the band structure as it promotes electron-hole recombination. The g-C_3N_4 has band gap that falls in visible light wavelength and therefore coupling with BiOBr would benefit to use larger fraction of solar light.[90] The hollow microsphere morphology of BiOBr was completely destroyed when grown over the surface of g-C_3N_4 sheets under wet-chemical approach. The composite was selective to produce CH_3OH from CO_2 at the optimized content of g-C_3N_4.[90] Liu *et al.* synthesized BiOBr/C_3N_4 by ultrasonicating the synthesized BiOBr and C_3N_4 for 6 h.[91] BiOBr was

View Article Online
DOI: 10.1039/D5LF00154D

synthesised by solvothermal technique and the oxygen vacancy was introduced by adding the surfactant along with precursors. Furthermore, oxygen vacancy can be introduced to BiOBr by adding the surfactant in solvothermal synthesis which is not possible in hydrothermal synthesis. The g-C_3N_4 heterojunction was constructed with BiOBr possessing surface oxygen vacancy. The morphology has been compared in figure 4.[91] Along with heterojunction interface, the presence of surface oxygen vacancy has promoted the charge separation and hence photocatalytic performance was enhanced.

Xi *et al.* also synthesized BiOBr/Bi_2S_3 and conducted a detailed analysis on the growth mechanism of Bi_2S_3 nanoarrays on BiOBr nanoplates.[92] Facet sensitive growth of Bi_2S_3 can be used as an effective strategy to construct a heterojunction with increased number of active sites using thioacetamide as the sulfur source. It can also be observed that the structurally a very close matching of the lattice parameters *c*-axis of Bi_2S_3 and *a* or *b* axis of BiOBr facilitates the facet selective growth of Bi_2S_3.[92] The established S-scheme heterointerface between BiOBr and Bi_2S_3 and produced 20.32 μmol g^{-1} CO from CO_2 photoreduction.[92] The large area exposure of both semiconductors helps in exploiting maximum amount of visible light. Directional growth of Bi_2S_3 as mesh like nanostructure on the surface of the BiOBr nanoplates *via* topotactic transformation process.[92]

Vertically aligned Bi_2S_3 nano walls help in minimal shielding of the light falling on the surface of BiOBr nanoplate substate which extends the optical response to 1000 nm (Figure 5). Authors have demonstrated that vacancy rich BiOBr substrate enhances the adsorption of CO_2 on the surface.[92] Due to weak Bi-O linkage, it is easy to produce oxygen vacancy in BiOBr. Since oxygen vacancy creates trap centres for photogenerated charge carriers, it enhances the separation efficiency. Rational design of oxygen vacancy rich BiOBr heterojunction would be beneficial in elevating the photocatalytic CO_2 reduction.

View Article Online
DOI: 10.1039/D5LF00154D

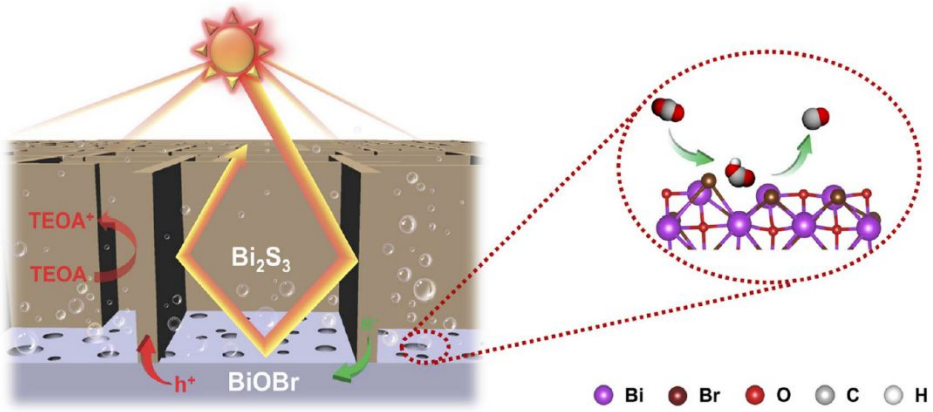

Figure 5. Schematic illustrating the proposed mechanism for the photocatalytic CO_2 reduction over the BiOBr/Bi_2S_3 heterojunction. Reproduced with permission from ref. 92. Copyright 2022, Royal Society of Chemistry.

Ma *et al.* suggested that instead of constructing the conventional heterostructures, co-sharing atoms can be effective strategy for interfacial engineering along with suitable band structure. This work stresses on the atom level interfacial contact of the heterostructures.[93] BiOBr is coupled with Bi_2S_3 a layered structure which delivers full spectrum responsive S-scheme photocatalyst. BiOBr/Bi_2S_3 was fabricated by *in situ* ion exchange method, which yielded Bi_2S_3 nanorods on BiOBr nanosheets. It is observed that the morphology of BiOBr nanosheets changed after reacting with sulphur atoms in hydrothermal reaction which indicates the occurrence of ion exchange reaction led to the formation of the heterojunction. It is also noted that as the sulphur concentration increases the density of Bi_2S_3 nanorods on BiOBr nanosheets. BiOBr/Bi_2S_3 heterostructure yielded CO with 20.32 μmol g^{-1}.

Bi_2WO_6 a layered structure, comprising of fluorite like $[Bi_2O_2]^{2+}$ and perovskite like $[WO_4]^{2-}$. Owing to its strong oxidising capability of valence band, Bi_2WO_6 is extensively studied for photocatalytic applications. However, the performance is limited by severe recombination of the photogenerated charge carriers. Therefore, composite of Bi_2WO_6 and BiOBr would

View Article Online
DOI: 10.1039/D5LF00154D

enhance the photocatalytic conversion of CO_2 reduction.[94] It is known from the literature that the surface oxygen vacancy can easily be created on Bi_2WO_6 and BiOBr which can provide increased number of adsorption sites for the reactants and trap states for the photogenerated charge carriers.[68, 95] Apart from oxides and sulphides, layered double hydroxides (LDH) were also used for making the composites with BiOBr. The CoAl-LDH has high selectivity towards CH_4 whereas NiAl-LDH yields CO.[96] As CoAl-LDH has suitable band positions with BiOBr, facile electron hole pair separation is possible. The heterojunction was fabricated by hydrothermal method. The optimal amount of ultrathin CoAl-LDH loaded on BiOBr has improved the selectivity towards CH_4, a value-added chemical.[96] In most of the cases, pristine BiOBr yields CO from photocatalytic conversion. In order to obtain value added products such as CH_4, the *p*-type semiconductor Cu_2O was heterojunctioned with BiOBr.[97] Recent studies have found that using metallic Bi found to be beneficial in enhancing the photogenerated charge separation.[14, 98, 99] Many reports claim that Bi-BiOBr show enhanced performance towards CO_2 photoreduction.[100] Rich oxygen vacancy can be successfully synthesized by *in situ* partial ion-exchange method on the heterojunction materials.[74] More importantly, metallic Bi self-doped Bi_2SiO_5 synthesized by hydrothermal method can provide facile situation for S-scheme heterojunction and thereby increase the redox capability in S-scheme BiOBr-(001)/Bi_2SiO_5/Bi heterojunction which gives CO production rate of 234.05 μmmol $g^{-1}h^{-1}$.[74]

AgBr is another excellent photo-response material, but it suffers from instability due to reduction of silver ion to metallic silver upon exposure to the light. The low electron-hole recombination and extended visible light response was achieved in BiOBr/AgBr.[101] Density functional theory and experimental results have demonstrated that electron depletion region is produced on BiOBr whereas electrons accumulate on AgBr resulting in S-scheme heterojunction to produce CO and CH_4. As intensity of the light increases the production of CO and CH_4 increases linearly proving that the reaction follows first order kinetics.[101]

View Article Online
DOI: 10.1039/D5LF00154D

$BiOBr_xI_{1-x}$ was coupled with $BiPO_4$ to form *p-n* junction which was synthesized by solvothermal method.[102] This heterojunction exhibited increased photocatalytic activity compared to $BiPO_4$.[102] The 0D/2D $CsPbBr_3$/BiOBr grown under different conditions were selective to produce CO rather than CH_4.[103, 104] The oxygen vacancies in BiOBr modulated the adsorption and activation of CO_2 and highly negative conduction band position of QDs promoted the reduction reaction pathways. Recently, coupling of BiOBr with *p*-type NiO was reported to be active for CO_2 reduction to yield CO and CH_4.[105] It was proposed that adsorption of CO_2 on the composite surface forms carbonate species, which is converted to formic acid by capturing protons and electrons. The formic acid was successively transformed to formaldehyde, methanol and methane by continuous hydrogenation process. Alternatively, CO_2 was directly transformed into CO by hydrogenation and dehydration.[105] The conduction band of NiO is mainly derived from the orbitals of Ni which enables the accumulation of electrons at the Ni sites of NiO, which primarily serves as adsorption centres for CO_2.[105]

Among BiOX materials, BiOI exhibits narrowest band gap (~1.6 to 1.9 eV) which enhances the absorption of light in visible region. BiOI consists of alternative layers of $[Bi_2O_2]$ and iodine held by Van der Waal's force of attraction. BiOI, an indirect band gap semiconductor was heterojunctioned with a perovskite material to improve the interfacial charge separation. A direct band gap semiconductor caesium formamidinium lead halide perovskite ($Cs_{1-x}FA_xPbBr_3$) was coupled with nanosheets of BiOI nanomaterial.[106] It is worth noting that the heterojunction was created by stirring the solution of BiOI and perovskite nanocrystals due to the low surface energy of perovskite nanocrystals and strong interaction between Bi cation and perovskites's Br anion. Perovskite with cuboid structure is well decorated on the ultrathin nanosheets of BiOI as confirmed by SEM and TEM images. Authors have demonstrated the kinetic models in figure 6 and they claim that BiOI have more surface defects than that of perovskite $Cs_{1-x}FA_xPbBr_3$ (CF).[106] However, when BiOI and CF were heterojunctioned, the

View Article Online
DOI: 10.1039/D5LF00154D

blue side of the photoinduced absorption band (PIA) becomes allowed transition with Bi^{3+} doping in CF. Internal electric field (IEF) is created due to the electron transfer between BiOI and CF which facilitates the recombination of electrons from the conduction band of the BiOI and holes of the valence band from CF perovskite to form S-scheme heterojunction as depicted in figure 6.

Formation of S-scheme was confirmed by X-ray photoelectron spectroscopy. Femtosecond transient absorption spectroscopy was utilized to investigate the ultrarapid dynamics of charge carriers. Doping of Bi^{+3} has created deep defect states at the interface which degraded the photocatalytic activity of CO_2 reduction.

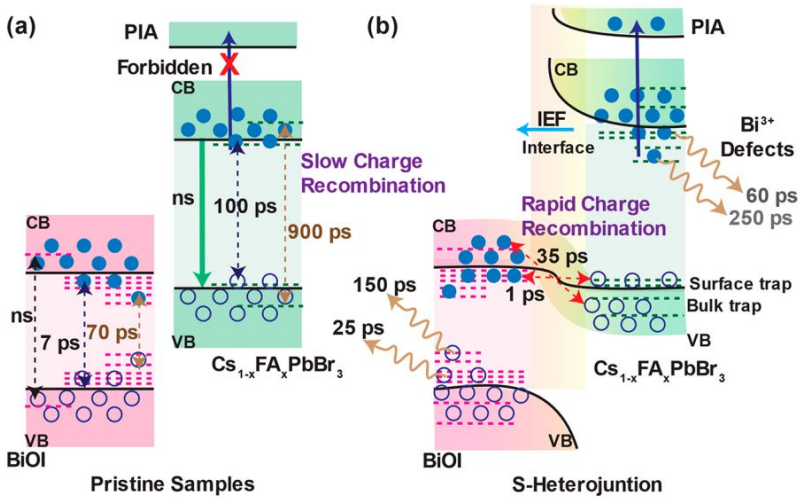

Figure 6. (a) Depiction of kinetic models for (a) pristine BiOI and $Cs_{1-x}FA_xPbBr_3$ (CF) and (b) hybrid $Cs_{1-x}FA_xPbBr_3$:BiOI (CF:BiOI) heterojunction samples. IEF represents internal electric field generated in the heterojunction. Reprinted with permission from ref.106. Copyright 2022, American Chemical Society.

View Article Online
DOI: 10.1039/D5LF00154D

In another work, BiOI nanosheets and In_2O_3 were synthesized individually by solvothermal technique.[107] Similar to the above work, heterojunction was formed by mixing the as synthesized semiconductors and heating solvothermally to obtain the heterojunction of BiOI/In_2O_3. The spherical morphology of In_2O_3 was decorated on the nanosheets. However, it is observed that the morphology was non-uniform throughout the heterojunction material. It can be inferred that heterojunction fabricated from solvothermal technique from taking the individual semiconductor materials yielded aggregation of In_2O_3 on BiOI nanosheets.[107] The BiOI/C_3N_4 constructed on hydrophobic carbon fiber paper through electrophoretic deposition process exhibited significant selectivity for CO production from CO_2 reduction reaction.[108] Initially, pre-formed g-C_3N_4 sheets and iodine powder were dispersed in acetone solvent, wherein protons were released upon reaction of iodine with acetone. Later, BiOI/carbon fiber and Pt electrodes was used as cathode and anode respectively, which was followed by application of external potential.[108] The BiOI-nanosheets were vertically grown on the surface of carbon fibers and g-C_3N_4 sheets completely wrapped the fibers to form 2D/2D contacts between the semiconducting surfaces.[108]

Authors have carried out interfacial engineering with the formation of *p-n* junction by compositing BiOI and Zn_2TiO_4.[109] The presence of oxygen vacancies speeds up the CO_2 reduction process.[110] It extends the lifetime of the charge carrier and also acts as activation sites to enhance the adsorption of CO_2. Wang *et al.* have fabricated 2D/2D Bi_2MoO_6/BiOI S-scheme heterojunction to enhance the photoreduction of CO_2.[110] BiOI nanosheets were grown on few layered Bi_2MoO_6 nanosheets using solvothermal technique. S-scheme mechanism was investigated by utilizing time resolved photoluminescence spectra, work function and charge density difference analysis. Nanosheets of Bi_2MoO_6 on BiOI nanospheres demonstrated that the Van der Waal's heterojunction is effective in accelerating the photogenerated charge

carriers. Authors have established that the charge transfer takes place from Bi_2MoO_6 to BiOI in addition to large area Van der Waal's heterojunction and S-scheme heterojunction.[110] Hongyu Fu *et al.* have synthesized the heterostructure of Cu_2O and carbon loaded BiOI using two steps methods.[111] The yield of methanol and ethanol from CO_2 was 722.8 μmol g^{-1} for 8 h. Photocatalytic performance of C-BiOI was significantly increased compared to pristine BiOI. Heterostructure of Cu_2O and carbon loaded BiOI further improved the photocatalytic activity. Cu_2O is a *p*-type semiconductor with the band gap of 2.2 eV. Nanoparticles of Cu_2O were decorated on to the nanosheets of C-BiOI by chemical deposition method. The introduction of Cu_2O remarkably increased the photogenerated charge carriers and also the surface area of the heterostructure which provided more active sites for CO_2 reduction.[111]

BiOI based 2D-2D heterojunction materials have been designed in order to elevate the photocatalytic performance. Band structure of C_3N_4 and BiOI is favourable to form S-heterojunction, which can boost the charge separation.[71] Li *et al.* have proposed S-scheme charge transport which increases the redox capability of both BiOI and C_3N_4 and converts CO_2 to CO.[112] Formation of S-scheme heterojunction facilitates the electrons to move from C_3N_4 to BiOI creating depletion region in C_3N_4 whereas electron accumulation occurs at BiOI. In order to develop wide wavelength responding photocatalysts, authors have interfaced In_2O_3 with BiOI as In_2O_3 exhibits band gap of 2.8 eV which falls in the visible region. It is also known to possess good electronic conductivity and resistant to corrosion. Type-II heterojunction was fabricated by solvothermal method.[107] In_2O_3/BiOI produces CO and CH_4.[72] 2D heterojunction of an atomic thin BiOI/BiOCl was constructed to mitigate the charge recombination. Oxygen – iodine binary vacancy was created which decreased the oxidation energy barrier and formed *COOH, a stable rate limiting intermediate.

View Article Online
DOI: 10.1039/D5LF00154D

3.2 $BiVO_4$

As there is a larger difference in the reduction potential for CO_2 and the conduction band potential of $BiVO_4$, only few studies are available on pure $BiVO_4$ towards the photocatalytic reduction of CO_2. It is found that $BiVO_4$ can selectively convert CO_2 to ethanol. In order to improve the photocatalytic performance, several strategies is adopted such as morphology control, doping with metals and defect introduction.[56, 113] It is found from the literature that metal nanoparticle doping can effectively tune the band gap of $BiVO_4$ and there by improve the selectivity and conversion efficiency.[113, 114] The high performing $BiVO_4$ quantum dots with Au nanoparticles were fabricated and heterojunctioned with rutile nanorod arrays.[115] The surface plasmon resonance of Au has not only helped in boosting the charge separation but also increased the light response of the photocatalyst.[116, 117] This led to the prolonged life time of the charge carriers and the increased separation efficiency. Similar approach was adopted to construct Z-scheme $BiVO_4$-Au-Cu_2O, where $BiVO_4$ (010)-Au provides Schottky junction and promotes electron extraction from $BiVO_4$.[118] In order to tune the electronic band structure of $BiVO_4$, Duan *et al.* co-decorated $BiVO_4$ with Ag and Bi nanoparticles.[119] Hollow microstructures of Bi/$BiVO_4$ which was synthesized by solvothermal method showed enhanced performance for the conversion of CO_2 to CO. To further improve photocatalytic reduction towards CO, metallic Ag nanoflakes were loaded on Bi/$BiVO_4$. The increased performance is mainly due to extended visible light response and enhances separation efficiency. Increased attention has been given to copper to substitute noble metals as it also increases the photocatalytic performance as copper acts as a hole/electron mediator which facilitates charge separation and improve the photocatalytic performance.[120] Wei Copi fabricated the composites of $BiVO_4$ and CdS and found increase in the photocatalytic activity towards CO_2 reduction.[121] The 2D-$BiVO_4$ has also been heterojunctioned with perovskites 2D-$CsPbBr_3$ to achieve high efficiency towards CO formation without any co-catalysts or sacrificial agents (Figure 7).[122]

View Article Online
DOI: 10.1039/D5LF00154D

The preparation step involved the heterogeneous nucleation of $CsPbBr_3$-sheets on the surface of $BiVO_4$ through annealing step in inert atmosphere, which outlines the stability of $BiVO_4$ as the substrate surface. The presence of oxygen vacancies in $BiVO_4$ achieved a gradient Fermi level shift, and enlarges the Fermi level gap between the semiconductors. This process is accompanied with enhanced interfacial electric field in the heterojunction, which consecutively promoted the charge carrier separation process. It was interesting to note that pure $CsPbBr_3$ had a quasi-square morphology with random sizes, while uniform nanosheets were grown on the $BiVO_4$ substrate surface, which further emphasize the pivotal role of substrate surface in altering the morphological features during the nucleation process.[122]

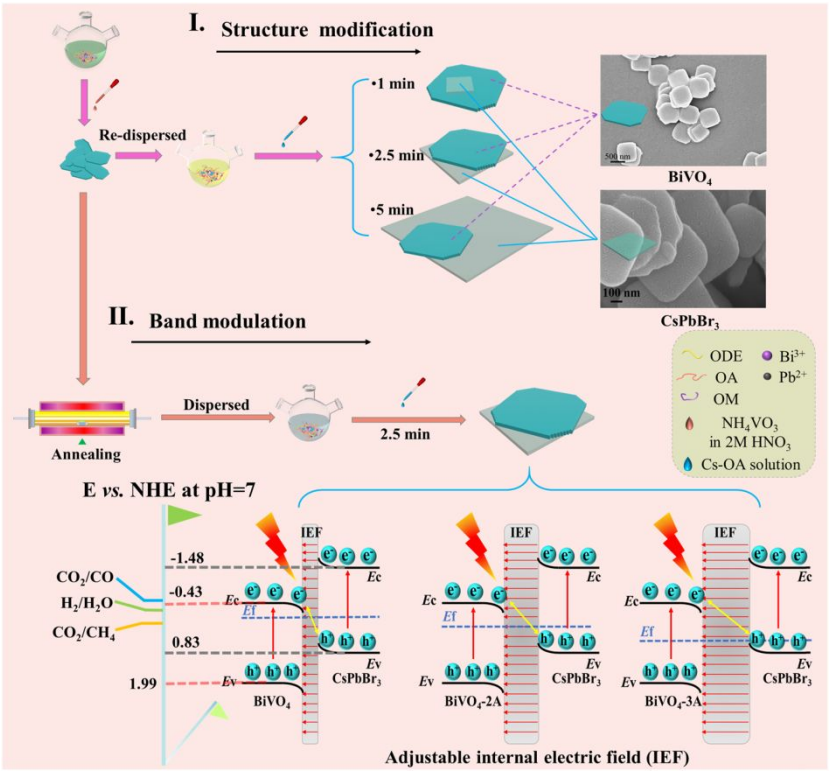

Figure 7. Schematic illustration of the synthesis, structural modification and band modulation of the $BiVO_4/CsPbBr_3$ heterojunction. Reprinted with permission from ref.122. Copyright 2022, Elsevier.

Wang *et al.* further explored from the synthesis of $Bi_2S_3/BiVO_4$ heterostructure which was obtained from in situ selective ion exchange method. Authors loaded the cocatalyst MnO_x on

View Article Online
DOI: 10.1039/D5LF00154D

the heterojunction photocatalysts to improve the selectivity.[60] In this work, photooxidation deposition method was adopted to decorate MnO_x facet selectively. $BiVO_4$ was synthesized by hydrothermal method and Bi_2S_3 nanosheets were preferentially grown on (110) of $BiVO_4$. Bi_2S_3 was grown on (110) of the $BiVO_4$ by sulphurisation. As the concentration of S^{2-} ions increases, surface of $BiVO_4$ turns rough as VO^{3-} ions will be replaced by S^{2-} since the solubility of Bi_2S_3 is more than $BiVO_4$. It is worth to note that if the reaction time is less than 90 minutes, the crystallinity of Bi_2S_3 was poor and structurally unstable. Therefore, effective interfacial contact will be unsuccessful in the short duration of the reaction.[60] However, as the time duration progresses to 120 minutes, the reaction will promote non-selective epitaxial growth. The sponge like structure of MnO_x grows selectively on (110) facets of $BiVO_4$ rather than on (010) facets of Bi_2S_3 nanosheets.[60] Photocatalytic reduction of CO_2 to CH_3OH was observed in this heterostructure with the production rate of 20 ± 2.33 $\mu molg^{-1}h^{-1}$.

Type-II heterojunction of $Bi_4Ti_3O_4$ with $BiVO_4$ was fabricated through simple electrospinning technique and solvothermal method.[123] $Bi_4Ti_3O_4$ with $BiVO_4$ formed Type-II heterojunction which yielded various intermediates to give CO and CH_4OH (Figure 8). Direct S-scheme heterojunction was formed between $BiVO_4$ and TiO_2 which changed the charge separation. Platinum decoration was carried out to enhance the CO_2 photoreduction. Platinum decoration on the surface of these catalysts helped in converting CO_2 to CH_4 by mitigating electron hole pair recombination.[124]

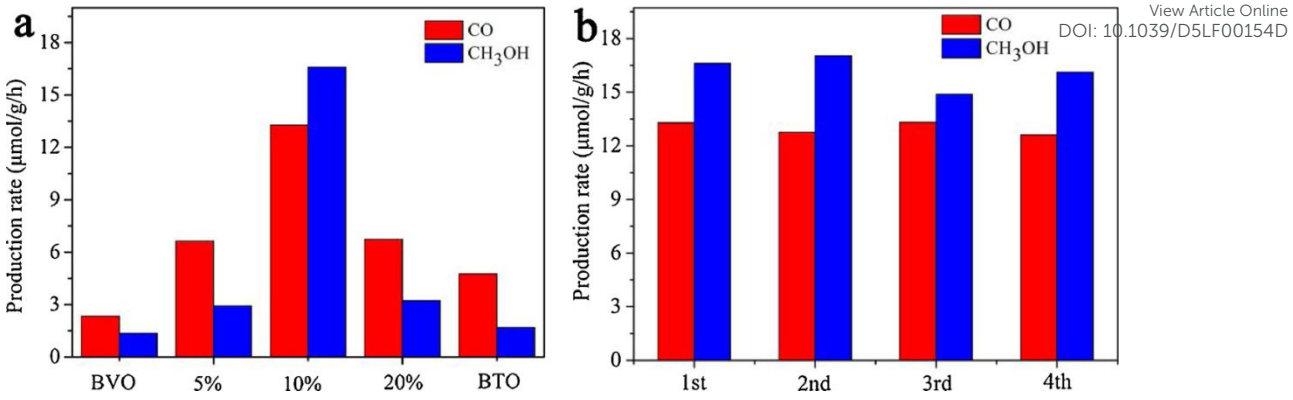

Figure 8. (a) CH_3OH and CO evolutions on the $BiVO_4/Bi_4Ti_3O_{12}$ with different $Bi_4Ti_3O_{12}$ content (b) photocatalytic activity stability of the $BiVO_4$/10 % $Bi_4Ti_3O_{12}$ sample. Reprinted with permission from ref.123. Copyright 2020, Elsevier.

S-scheme heterojunction was fabricated by growing $BiVO_4$ on the surface of a metal organic framework PCN-224 (Cu). This photocatalyst exhibited 100% CO selectivity. Z-scheme heterojunction of $BiVO_4$ and Bi_2S_3 was constructed and MnO_x catalyst was selectively decorated on the surface of (110) facet of $BiVO_4$ by photodeposition technique. Liu *et al.* has decorated Co-Pi, a cocatalyst on $BiVO_4/SnO_2$ and coupled with Au cathode to achieve better conversion efficiency for CO_2.[125] The Z-schematic pathway for charge carriers were constructed using $SrTiO_3$: Rh and $BiVO_4$.[126] In this work, powder of the photocatalyst was used without adjusting the pH. It is worth noting here that the conversion of CO_2 to CO was progressed without any addition of additives.

3.3 Bi_2WO_6

Bi_2WO_6 belonging to an Aurivillius family of oxides has been widely researched for its photocatalytic activity owing to its structure, composition and electronic property. Due to the presence of $[Bi_2O_2]$ and perovskite type layers, Bi_2WO_6 possesses narrow band gap which is around 2.6 eV. Due to sluggish reaction kinetics and high rate of recombination of

View Article Online
DOI: 10.1039/D5LF00154D

photoinduced charge carriers, photocatalytic performance is poor.[127] Therefore, in order to improve the photocatalytic activity, several modifications have been made to Bi_2WO_6 such as morphology control, heterojunction construction and doping.[128] It is important to have an update on the recent works for Bi_2WO_6 to design any new material or to modify the existing photocatalyst. As the band gap of Bi_2WO_6 is wider and unable to utilize the maximum visible light, the heterojunction is constructed with other semiconductors such as $Cs_3Bi_2Br_9$, TiO_2, Cu_2O, $InVO_4$, C_3N_4, BiOBr and BiOI.[129-133]

NiO with narrow band gap ~2.5 eV which can efficiently absorb visible light is composited with Bi_2WO_6 which gives a S-scheme charge transfer. The heterojunction yielded CO and CH_4 with 46.9 and 12.1 μmol g^{-1} with CO* intermediate.[134] Lulu Zhao *et al.* attempted to improve the selectivity of the catalyst towards CO from CO_2 by substituting Bi^{3+} and Ag^+ ions through liquid phase exchange process.[135] Incorporation of Ag^+ not only improved the adsorption of CO_2 and H_2O but also enhanced the separation of the charge carriers.[135] Ultrathin Bi_2WO_6 nanosheets with Ag^+ and Bi^{3+} exhibits conversion of CO_2 to CO with yield 116 μmol g^{-1} with the selectivity of 95.7 % after 6 h reaction without using any sacrificial agents. The insitu DRIFT suggested that the intermediate formed is COOH* which then converted to thermodynamically stable CO*. It was possible to obtain methane from CO_2 photoreduction from Bi_2WO_6 by modifying the surface with surface plasmon resonance. Precisely controlling the oxygen vacancy in Bi-O-Bi and W-O-W lead to high selectivity towards CH_4. The vacancy created an energy level which is very close to conduction band helped in improving the life span of the charged carriers. To further improve the charge transport pathway, Bi_2WO_6 was covalently heterostructured with Bi_2O_3. Bi_2O_3 nanosheets present on the Bi_2WO_6 surface renders more active sites for which enhances the adsorption of CO_2 on the surface.

Graphdiyne (GDY) is explored as a potential material for solar energy harvesting since its first synthesis.[136, 137] Ultrathin heterojunction of GDY and Bi_2WO_6 was prepared by simple

hydrothermal method as GDY is an excellent material for efficient charge transfer.[138] Also, increased surface area helped in improving the CO_2 adsoprtion on the photocatalyst. GDY/Bi_2WO_6 yielded f 2.13 and 0.23 μmol h^{-1} g^{-1} of CH_3OH and CH_4 respectively. The reduction of CO_2 performance yielded CH_3OH and CH_4 (Figure 9).[138]

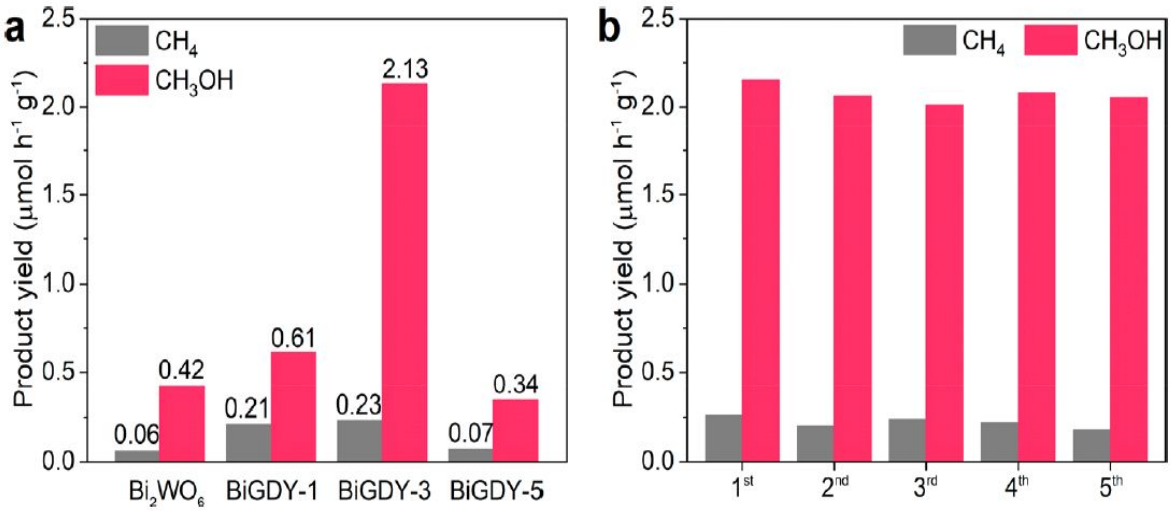

Figure 9. (a) Photocatalytic CO_2 reduction performance of samples. (b) Cycling tests of GDY/Bi_2WO_6 heterojunction (BiGDY). Reproduced with permission from ref.138. Copyright 2021, American Chemical Society.

Further, to enhance the light absorption ability of the material, hierarchical hollow structured heterojunction of Bi_2WO_6/TiO_2 was constructed by in situ synthetic technique. This heterojunction interface generated the $Bi^{(3-x)+}$ active site which can suppress the charge carriers' recombination very effectively. In producing CO from CO_2 photoreduction, this heterojunction was better than that of pristine Bi_2WO_6 and Bi_2WO_6/TiO_2.[27] Similarly, Bi_2WO_6 was heterojunctioned with other semiconductors such as $InVO_4$, $La_2Ti_2O_7$, ZnV_2O_6 either to improve the light absorption ability or to suppress the recombination rate of electron hole pairs.[139-141]

View Article Online
DOI: 10.1039/D5LF00154D

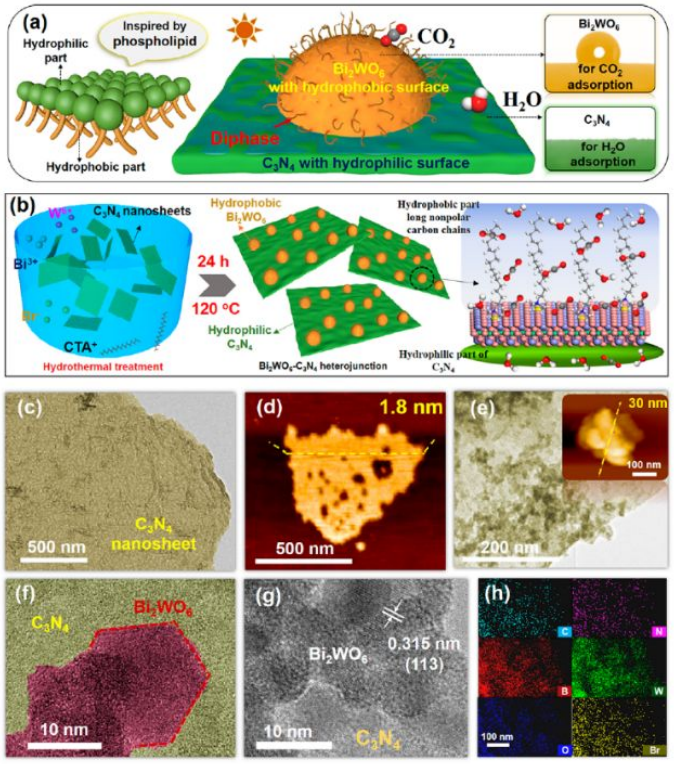

Figure 10. (a) Schematic of the hydrophobic Bi_2WO_6-hydrophilic C_3N_4 photocatalyst and distribution of CO_2 and H_2O. (b) Schematic of the preparation of a phospholipid-mimicking photocatalyst. (c) TEM images and (d) AFM image of C_3N_4. (e) TEM image and AFM image (inset) of Bi_2WO_6-CN. (f and g) HR-TEM images of Bi_2WO_6-C_3N_4. (h) EDS elemental mapping of Bi_2WO_6-C_3N_4. Reproduced with permission from ref. 143. Copyright 2024, American Chemical Society.

Qiaoya Tang *et al.* constructed a S-scheme heterojunction of C_3N_4/Bi_2WO_6 using electrostatic self-assembly method.[142] Authors claim that the formed ultrathin 2D/2D C_3N_4/Bi_2WO_6 heterostructure offers abundant reaction sites which promoted efficient charge transfer. Yunpeng Liu *et al.* introduced hydrophobic and hydrophilic ends in the diphasic photocatalyst to solve the competitive adsorption issue of CO_2 and H_2O. This amphipathic diphasic hydrophobic and hydrophilic photocatalyst not only inhibits the recombination of

View Article Online
DOI: 10.1039/D5LF00154D

charge carriers but also it can enrich CO_2 and H2O on hydrophobic and hydrophilic surfaces respectively as depicted in Figure 10.[143]

In an effort to improve the yield of CH_4 in CO_2 photoreduction, Yan-Yang Li *et al.* modified Bi_2WO_6 with chloride ions in view of considering proton produced during the water oxidation affecting the CH_4 generation.[144] Density functional theory confirmed that the mappings of Bi_2WO_6-C_3N_4. chloride ions present on the surface of Bi_2WO_6 nanosheets not only promoted water oxidation but also favoured the formation of CHO* intermediate which facilitated the formation of CH_4. Due to the presence of chloride ions on the surface, the rate of oxidation half reaction goes smoothly which indirectly promotes reduction half reaction (CO_2 reduction).[144] As 2D/2D nanosheets provide large specific surface area and rich active sites, Yong Jiang *et al.* fabricated the heterojunction of $Cs_2AgBiBr_6/Bi_2WO_6$.[145] This enabled Z-scheme charge transfer and reduced charge carrier recombination to obtain the yield of 1582.0 μmol g^{-1} for CO and 8602 μmol g^{-1} of CH_4.[145]

Black phosphorous (BP) is a 2D material which is considered as a potential candidate for photocatalytic applications as it provides short diffusion length for the charge carriers. Since BP has large specific area, it offers ample reaction sites for CO_2 adsorption. Therefore, BP has been used for constructing heterojunction with Bi_2WO_6 as it is believed to accelerate multistep electron process and dimerization of C-C bond. Minghui Zhang *et al.* fabricated 2D/2D BP/Bi_2WO_6 by electrostatic assembly method.[146] Organic oxidation to value added product was coupled with CO_2 reduction which lowers the thermodynamic barrier for water oxidation. In this regard, benzylamine which is a derivative of the renewable biomass was used for organic oxidation to give imines as high value product. The adsorption study revealed that Bi_2WO_6 with BP exhibited more active sites for CO_2 adsorption. In addition to this, benzylamine provided alkaline media which increases the solubility of CO_2 in the solution. In situ Fourier transform infrared radiation (FTIR) suggested CO* and CH_3* are the intermediates for the

View Article Online
DOI: 10.1039/D5LF00154D

conversion of CO_2 to C_2H_5OH.[135] To harvest visible light absorption and to improve charge transfer, g-C_3N_4 was introduced on Bi_2WO_6. The photocatalytic performance was further enhanced by incorporating reduced graphene oxide.[142, 147] In another report, ultrathin 2D/2D Bi_2WO_6/g-C_3N_4 offered abundant contact interfaces with more accessible reaction sites that exhibited higher selectivity for CO generation compared to CH_4. The higher content of Bi_2WO_6 hampered the performance of the composite, as they can shield the incident photons striking the catalyst surface and hinder the bandgap excitation process. Furthermore, composite retained its performance even after four consecutive cycles.[142] These 2D/2D heterojunction with face-to-face interfaces can lower the intrinsic resistance and boost the charge carrier separation process.[148]

The deposition of QDs like $Cs_3Bi_2Br_9$ on the Bi_2WO_6-nanosheets can selectively promote the CO_2 reduction reactions to form CO under the visible light.[133] This unique 0D/2D (dot-to-face) geometry and lead free bismuth halide perovskite semiconductor remained as an added advantage for this composite. The larger surface area of 2D sheets enabled the finer distribution of QDs on its surface, which not only resulted in stable heterojunction but also lowered the distance for charge carrier migration process. The preparation method was flexible as it only involved the dispersion of positively charged QDs on the negatively charged sheets isopropanol suspension through electrostatic self-assembly approach. This strategy has benefit from the prospect of retaining the pristine morphology of concerned semiconductors during the heterojunction formation. The ESR analysis revealed the generation of both hydroxyl and superoxide radicals, which further confirms the formation of S-scheme heterojunction between them.[133]

3.4 Bi_2MoO_6

Bi_2MoO_6 is also found to be an interesting material which belongs to Aurivillius oxide family. The structure of Bi_2MoO_6 consists of alternating array of $[Bi_2O_2]$ and $[MoO_6]$ octahedra

layers. This ternary metal oxide is an *n*-type semiconductor possessing narrow band gap which can utilize visible light of the solar spectrum.[149, 150] It is possible to effectively tune the electronic distribution and morphology to optimize the photocatalytic application towards CO_2 reduction. By changing the temperature, reaction time and solvent, it is easier to modify the morphology of Bi_2MoO_6. Therefore, enormous effort has been put to improve the photocatalytic performance of Bi_2MoO_6 by morphology control and heterojunction composite. Dai *et al.* has grown Bi_2MoO_6 quantum dots on reduced graphene oxide scaffolds using economically viable hydrothermal method.[151] Due to high surface area of reduced graphene oxide, dispersion of Bi_2MoO_6 quantum dots was enhanced. The electron migration from Bi_2MoO_6 quantum dots to reduced graphene oxide was facile as reduced graphene oxide exhibits excellent electrical conductivity. The photocatalytic mechanism is illustrated in Figure 11.

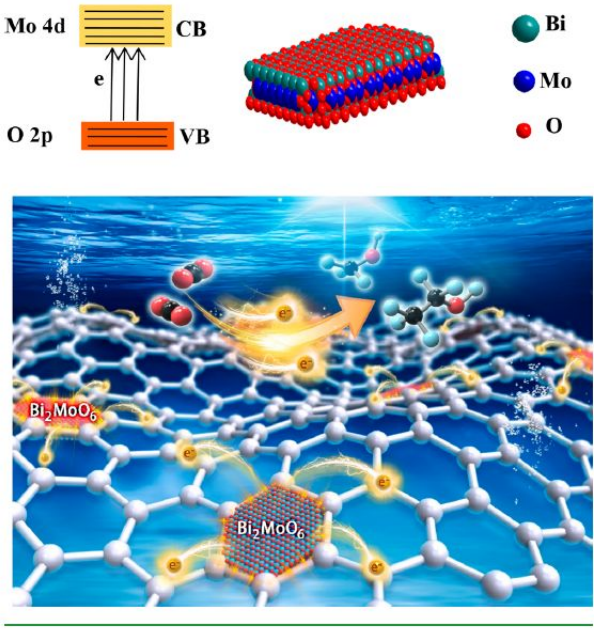

Figure 11. Unit cell model of Bi_2MoO_6, and electron Transfer. Reproduced with permission. Reprinted with permission from ref.151. Copyright 2020, American Chemical Society.

View Article Online
DOI: 10.1039/D5LF00154D

Yu *et al.* has fabricated hierarchical heterostructure of 2D nanosheets of Bi_2MoO_6 was grown on 1D In_2S_3 using solvothermal technique. Hollow nanotubes of In_2S_3 nanostructure were designed using MIL-68 precursor. The surface oxygen vacancy was created by using N,N,N',N'-Tetramethylethylenediamine (TMEDA). However, the morphology of Bi_2MoO_6 nanosheets get distorted to give particle like morphology if TMEDA is used to introduce surface oxygen vacancy.[152] The presence of interfacial Mo-S bond in $Bi_2MoO_6/ZnIn_2S_4$ boosted the production of CO from CO_2 reduction reactions.[150] The in-situ loading of $ZnIn_2S_4$ nanoflakes on the porous microspheres of Bi_2MoO_6 under the solvothermal conditions, offered plentiful catalytic sites for CO_2 adsorption and activation process. Furthermore, the hierarchical structures enhanced the visible light absorption and also possessed good photostability and reusability. The generation of superoxide and hydroxyl radicals as confirmed from the ESR analysis confirmed the formation of S-scheme heterojunction between them.[150] The oxygen vacancies engineered Bi_2MoO_{6-x}/MoS_2 was active for CO_2 reduction to form CO, wherein oxygen vacancies were obtained from pristine Bi_2MoO_6 through simple annealing step. It was interesting to note that the oxygen vacancies did not disrupt the microsphere-like morphology of the host matrix and density of oxygen vacancies increased upon composite formation with MoS_2-nanosheets. The presence of these oxygen vacancies lowered the bandgap of host matrix and act as effective electron pedals to delay the accumulation of charges and also reduces the work function of host matrix, which indirectly lessens the energy required for the electron transfer process.[153]

Maryam Ahmadi *et al.* heterojunctioned with the benchmark photocatalyst TiO_2 to reduce the rate of recombination of photogenerated electron-hole pair.[154] Synergistic effect was achieved by compositing Bi_2MoO_6 with TiO_2 as the band gap of both materials achieve staggered configuration. Bi_2MoO_6 nanosheets were decorated TiO_2 nanobelts by simple solvothermal method. As cocatalysts act as electron scavengers, Pt-Cu was decorated on the composite by

View Article Online
DOI: 10.1039/D5LF00154D

reduction method. It was noticed that the photo response of the photocatalyst has increased and obtained 34.6 μmol g^{-1} of methane for Bi_2MoO_6/TiO_2. Once the Pt-Cu were loaded on the composite, the methane production was increased further as cocatalyst help in trapping the electrons and reduce recombination rate.[154]

Other metal oxide semiconductor materials have also been heterojunctioned such as a spinal compound $ZnFe_2O_4$ which produced CO and CH_4.[155] The S-scheme pathway helped in slight improvement of the CO_2 reduction; the catalyst needs to be improved to achieve better photocatalytic performance. The 2D/2D $Bi_2MoO_6/Zn_3V_2O_8$ which formed S-scheme produced CO and CH_4.[156] The Ni containing metal organic framework (MOF) on Bi_2MoO_6 exhibits great potential towards photocatalytic CO_2 reduction. Similarly, Co-MOF has also been synthesized and found that the photocatalyst yields CO and CH_4.

Nanosheets, belts, particles and spheres of Bi_2MoO_6 have been synthesized, reports on quantum dots of Bi_2MoO_6 is uncommon.[157-159] Weili Dai *et al*. anchored quantum dots of Bi_2MoO_6 on 2D reduced graphene oxide (rGO) sheets which act as an electron reservoir helps in boosting the CO_2 reduction. Quantum dots Bi_2MoO_6/2D rGO produced 84.8 μmol g^{-1} of methanol and 57.5 μmol g^{-1} of ethanol which is highest among bismuth based photocatalyst towards reduction of CO_2. [151] Further, the quantum dots of Bi_2MoO_6 was deposited on the pomelo peel derived carbon (CPP) to improve the photocatalytic property of the catalyst. The CPP possesses high specific surface area and has excellent thermal conductivity. As the photothermal temperature increases, it not only enhances the migration rate of the electrons and holes but also promotes adsorption of CO_2. Mingnv Guo *et al.* synthesized 0D/3D CPP-A/Bi_2MoO_6 to achieve photothermal synergy to effectively utilize the solar spectrum.[160] As temperature increases up to 100 ℃, migration ability is increased and C-O-Bi bridge is formed which enhanced the electron transfer at the interface. This work would provide a solution for bottle neck problem of poor charge carrier transport in photothermal catalytic activity.[160]

View Article Online
DOI: 10.1039/D5LF00154D

Combining both *n*-type semiconductors In_2S_3 and Bi_2MoO_6, S-scheme was achieved to design an efficient photocatalyst. 2D nanosheets of Bi_2MoO_6 was grown on 1D nanotubes of In_2S_3 reduced the carrier diffusion length. Z-scheme heteorjunctions such as Bi_2MoO_6/CdS, Bi_2MoO_6/CeO_2 have also been constructed to improve the charge carrier transport.[161, 162] S-Scheme heterostructure can also be achieved from $ZnIn_2S_4$ decorated on Bi_2MoO_6 where Mo-S bond at the interface helped in improving the photocatalytic activity.[150] S-scheme heterostructures can also be achieved by chalcogenides, especially with MnS. Diethylenetriamine (DETA) ammonia treated MnS hollow sphere heterostructured with Bi surface plasmon resonance enhanced CO_2 reduction rate of Bi_2MoO_6. The presence of basic functional groups on DETA reduced the activation energy of acidic CO_2 whereas surface plasmon effect from Bi produces hot electrons and decreases the recombination rate of charge carriers. This combined effect helped in boosting the CO_2 photocatalytic reduction reaction.

Table 1. Comparison of heterojunction of bismuth-based materials and their photocatalytic conversion of CO_2 along with synthesis technique.

Bismuth based material	Preparation Method	Nature of hetero-junction	Products: Production Rate in $\mu molg^{-1}h^{-1}$	Reference
BiOCl/BiOBr	Hydrothermal Temperature - 160 ℃ Time - 12 h	Type-I	CO: 7.353	84
Bi_2WO_6/TiO_2	Solvothermal	Type-II	CO: 43.7	27
$BiOCl/Bi_2WO_6$	Hydrothermal Temperature - 120 ℃ Time - 12 h	Type-II	CO: 6.63	76
$BiOBr/Bi_2S_3$	Hydrothermal Temperature - 180 ℃	Type-II	CO: 103,500	92

View Article Online
DOI: 10.1039/D5LF00154D

	Time - 2 h			
BiOBr/CoAl LDH	Hydrothermal Temperature - 160 ℃ Time - 12 h	Type-II	CO: 4.096 CH_4: 4.174	96
$BiOI/In_2O_3$	Hydrothermal method Temperature - 180 ℃ Time - 12 h	Type-II	CO: 11.98 CH_4: 5.69	107
$BiVO_4/Bi_4Ti_3O_{12}$	Hydrothermal Temperature - 160 ℃ Time - 21 h	Type-II	CH_3OH: 16.6 CO:13.29	123
$BiVO_4/Bi_2S_3/MnO_3$	Selective epitaxial growth Temperature - 180 ℃ Time – 90 mins	Z-scheme	CH_3OH: 20 ± 2.33	60
$BiOBr/HNb_3O_8$	Self-Assembly ultrasonic dispersion for 30 min	Z-Scheme	CO: 164.6	163
g-C_3N_4/BiOI/RGO	hydrothermal method Temperature - 160 ℃ Time - 6 h	Z-Scheme	CO: 21.85	164
Co-MOF/Bi_2MoO_6	Solvothermal followed by insitu growth method Temperature - 165 ℃ Time - 16 h	Z-scheme	CO: 19.76 CH_4: 8.24	165
$BiVO_4/Cu_2O/Bi$	Solvothermal Temperature - 120 ℃ Time - 6 h	Z-Scheme	CH_4: 1.8 CO: 8.4	166
In_2O_3/Bi_2S_3	Hydrothermal followed by ultrasonication Temperature - 180 ℃ Time – 24 h	Z-scheme	CO: 2.67	167

quinacridone/$BiVO_4$	self-assembly method Stirring for 1 h	Z-Scheme	CO: 407 CH_4: 29	168
$BiOCl/C_3N_4$	Hydrothermal Temperature - 120 ℃ Time – 12 h	Z-scheme	CO: 45.33	169
BiOBr-(001)/Bi_2SiO_5/Bi	Solvothermal method Temperature - 190 ℃ Time – 12 h	S-Scheme	CO: 234.05	74
$BiOBr/Bi_2WO_6$	Hydrothermal Temperature - 160 ℃ Time – 6 h	S-Scheme	CO: 55.17	94
$BiOBr/Cu_2O$	Hydrothermal Temperature - 160 ℃ Time – 12 h	S-scheme	CH_4: 22.78	97
$BiOBr/CsPbBr_3$	Self -assembly process Overnight magnetic stirring in dark.	S-scheme	CO: 104.4 CH_4: 10.0	103
$BiVO_4/CsPbBr_3$	In situ colloidal growth method	S-scheme	CO: 103.5	122
$Cs_3Bi_2Br_9$/Porous BiOCl	Dipping method Magnetic stirring for 1 h.	S-scheme	CO: 25.5	170
$BiVO_4$/Cu-Bi	Solvothermal Temperature - 120 ℃ Time – 6 h	Oxygen vacancy	CO: 2.96	56
$BiOCl/Br\text{-}O_V$	Solvothermal Temperature - 160 ℃ Time – 10 h	Defects	CO: 7.37	171

Note: Readers are requested to follow the respective references for more information.

Table 1 illustrates different interfacial engineering of bismuth-based materials with various other compounds and their respective CO_2 conversion product. The synthesis method and also

View Article Online
DOI: 10.1039/D5LF00154D

charge carrier pathway followed by the heterojunction is also mentioned. It is interesting to note that most of the bismuth-based materials are fabricated by wet-chemical approaches such as hydrothermal and solvothermal methods. However, these techniques pose several challenges, as the materials purity and morphology are sensitive to synthesis temperature and reaction time. Therefore, reproducibility of the structure-morphological features would be difficult for the large-scale synthesis.[172, 173]

Other bismuth containing materials such as $Bi_{12}O_{17}Br_2$/g-C_3N_4, $Bi_{12}O_{17}Cl_2$/g-C_3N_4, Bi_3NbO_7/g-C_3N_4, $SrBi_4Ti_4O_{15}/Bi_2O_3$, Cs_2CuBr_4/Bi_2O_3, $BiOIO_3$/CdS and $Bi/Bi_4V_2O_{11}$, are explored for CO_2 photocatalytic conversion.[174-181] In particular, the presence of interfacial Bi-N bonds and the nitrogen vacancy in $Bi_{12}O_{17}Br_2$/g-C_3N_4 achieved simultaneous tetracycline degradation and CO_2 reduction reactions.[175] In fact, photocatalytic reduction of CO_2 was improved in the presence of tetracycline compared to Rhodamine-B and phenol molecules, which was attributed to the superior electron donating ability of TC. The flower-like $Bi_{12}O_{17}Br_2$ were decorated on the defective g-C_3N_4 surface under the wet-chemical approach. The presence of defects was important to drive the coupled photocatalytic reactions. It was proposed that *CO_2 was transformed to *COOH through hydrogenation step, which upon further protonation yielded *CO which was feasible for the desorption from the composite surface. This work is a classical illustration of win-to-win strategy achieve both environmental and energy related issues.[175] Alternatively, $Bi_{12}O_{17}Cl_2$/g-C_3N_4 promoted the formation of CH_4 through two-electron and two-proton reaction pathways.[179] On the other hand, Bi_3NbO_7/g-C_3N_4 promoted the formation of CH_4 as the reduction pathway proceeded through the formation of CH_3O* and CHO* fragments.[176] Lee *et al.* reported CdS-nanorods/$BiOIO_3$-nanosheets (1D/2D) selectively generated CO and minor amounts of H_2 during the CO_2 reduction reactions and activity was retained even after four consecutive cycles.[180] The line interfacial contact between the integrated materials promoted the charge carrier lifetime with minimal recombination

View Article Online
DOI: 10.1039/D5LF00154D

pathways.[182] Significant improvement in photocatalytic performance was noticed, yet these materials must be explored further to enhance the conversion of CO_2 to value added product.

Conclusion and perspective

Photcatalytic reduction of CO_2 into the fuels and simple chemicals is a versatile approach that can simultaneously address the environmental issues, carbon neutrality and the energy demands. The high degree of chemical inertness of CO_2, sluggish dynamics of multi-electron reduction reactions and massive charge carrier recombination in single-phase photocatalytic active materials has driven the emergence of heterojunction photocatalysts. In this context, bismuth based materials found to be interesting class of material as they possess narrow band gap and favourable electronic structure for photocatalytic CO_2 reduction reaction. Although notable progress is achieved with Bi-based heterojunctions, the achieved efficiency is still far from the satisfactory, as the presence of single electric field may not always boost the charge carrier separation process. Thus, future research must essentially focus on the coupling of multiple electric fields, which not only extend the carrier life time, but also allows their diffusion to react with the adsorbed species. Furthermore, design and fabricating the hierarchical Bi-based heterojunctions comprising QDs, 1D, 2D and 3D forms would be even more advantageous from the prospect of improving the light harvesting capacity, surface reactions and charge carrier separation kinetics. In addition, some importance should be given for the preparation of NIR responsive Bi-based materials, which would spotlight our interest to harvest the complete solar light for the photocatalytic reactions. From the viewpoint of charge carrier dynamics, steering the migration of charge carriers in a specific path without compromising their lifetimes requires a suitable interface during the fabrication of heterojunctions. Alongside, coupling of CO_2 reduction reaction with pollutant degradation, H_2O_2 generation and synthesis of organic compounds will full-fill our dream of achieving the win-to-win strategy comprising energy and environmental aspects.

This review summarizes the interfacial engineering carried out for bismuth-based materials in recent years for CO_2 reduction. A large number of reported works have demonstrated that the interfacial engineering helps to effectively enhance the charge separation, light absorption and adsorption of CO_2 on the surface of the photocatalyst. However, the conversion efficiency is far from efficiency required to implement in practical applications. Most of the interfacially engineered bismuth based photocatalysts exhibited the rate of reduction of CO_2 less than 100 μmol g^{-1}. It is also noticed from the previous literature that the product obtained from the photocatalytic reduction reaction is carbon monoxide. Though $BiVO_4$ shows promising results in photoelectrochemical water splitting, photocatalytic activity towards CO_2 reduction is insignificant even after interfacial engineering with several other competent materials. Therefore, attention must be paid to enhance the photocatalytic activity of bismuth-based materials to meet the practical requirements for photocatalytic CO_2 reduction.

Declaration of the competing interest

Authors declare that there is no competing financial interest.

Data Availability

No data used in this article.

References

1. B. Kumar, M. Llorente, J. Froehlich, T. Dang, A. Sathrum and C. P. Kubiak, *Annual Review of Physical Chemistry*, 2012, **63**, 541-569.
2. T. Abbas, H. S. M. Yahya and N. A. S. Amin, *Energy & Fuels*, 2023, **37**, 18330-18368.
3. R. Pang, K. Teramura, M. Morishita, H. Asakura, S. Hosokawa and T. Tanaka, *Communications Chemistry*, 2020, **3**, 137.
4. S. J. Cobb, S. Rodríguez-Jiménez and E. Reisner, *Angewandte Chemie International Edition*, 2024, **63**, e202310547.
5. U. Ulmer, T. Dingle, P. N. Duchesne, R. H. Morris, A. Tavasoli, T. Wood and G. A. Ozin, *Nature Communications*, 2019, **10**, 3169.
6. H. S. Shafaat and J. Y. Yang, *Nature Catalysis*, 2021, **4**, 928-933.

View Article Online
DOI: 10.1039/D5LF00154D

7. G. Gadikota, *Commun Chem*, 2021, **4**, 23.
8. B. Wang, S. Chen, Z. Zhang and D. Wang, *SmartMat*, 2022, **3**, 84-110.
9. D. H. Apaydin, *Israel Journal of Chemistry*, 2022, **62**, e202100085.
10. C. Zuo, Q. Su and X. Yan, *Journal*, 2023, **11**.
11. S. S. Bhosale, A. K. Kharade, E. Jokar, A. Fathi, S.-m. Chang and E. W.-G. Diau, *Journal of the American Chemical Society*, 2019, **141**, 20434-20442.
12. T. Zhao, J. Xiong, W. Li, G. Cheng and S. X. Dou, *Chemical Engineering Journal*, 2025, **506**, 160313.
13. D. K. Chauhan, N. Sharma and K. Kailasam, *Materials Advances*, 2022, **3**, 5274-5298.
14. S. C. Shit, I. Shown, R. Paul, K.-H. Chen, J. Mondal and L.-C. Chen, *Nanoscale*, 2020, **12**, 23301-23332.
15. E. Gong, S. Ali, C. B. Hiragond, H. S. Kim, N. S. Powar, D. Kim, H. Kim and S.-I. In, *Energy & Environmental Science*, 2022, **15**, 880-937.
16. T. Zhao, W. Zhang, J. Xiong, W. Li and G. Cheng, *Separation and Purification Technology*, 2025, **360**, 130849.
17. G. Yang, J. Xiong, M. Lu, W. Wang, W. Li, Z. Wen, S. Li, W. Li, R. Chen and G. Cheng, *Journal of Colloid and Interface Science*, 2022, **624**, 348-361.
18. W. A. Thompson, E. Sanchez Fernandez and M. M. Maroto-Valer, *ACS Sustainable Chemistry & Engineering*, 2020, **8**, 4677-4692.
19. S. G. Kumar, R. Kavitha and C. Manjunatha, *Energy & Fuels*, 2023, **37**, 14421-14472.
20. B. Tang and F.-X. Xiao, *ACS Catalysis*, 2022, **12**, 9023-9057.
21. W. Huang, Q. Zhu, Y. Zhu, C. Chen and J. Shen, *Materials Today Energy*, 2023, **38**, 101458.
22. Z. Dong, B. Li, Y. Zhu and W. Guo, *EES Catalysis*, 2024, **2**, 448-474.
23. L. D. M. Torquato, F. A. C. Pastrian, J. A. L. Perini, K. Irikura, A. P. de L. Batista, A. G. S. de Oliveira-Filho, S. I. Córdoba de Torresi and M. V. B. Zanoni, *Applied Catalysis B: Environmental*, 2020, **261**, 118221.
24. S. Wang, G. Wang, T. Wu, Y. Zhang, F. Zhan, Y. Wang, J. Wang, Y. Fu and J. Qiu, *Journal of Materials Chemistry A*, 2018, **6**, 14644-14650.
25. K. R. Rao, S. Pishgar, J. Strain, B. Kumar, V. Atla, S. Kumari and Joshua M. Spurgeon, *Journal of Materials Chemistry A*, 2018, **6**, 1736-1742.
26. Y. Xiao, A. Abulizi, K. Okitsu and T. Ren, *Journal of Industrial and Engineering Chemistry*, 2023, **125**, 317-324.
27. W.-R. Liu, S. Yu, Z. Liu, P. Jiang, K. Wang, H.-Y. Du, Z.-Y. Hu, M.-H. Sun, Y.-L. Wang, Y. Li, L.-H. Chen and B.-L. Su, *Inorganic Chemistry*, 2024, **63**, 6714-6722.
28. Y. Ma, X. Yi, S. Wang, T. Li, B. Tan, C. Chen, T. Majima, E. R. Waclawik, H. Zhu and J. Wang, *Nature Communications*, 2022, **13**, 1400.
29. A. Sharma, A. Hosseini-Bandegharaei, N. Kumar, S. Kumar and K. Kumari, *Journal of CO2 Utilization*, 2022, **65**, 102205.
30. J. Wu, Y. Huang, W. Ye and Y. Li, *Advanced Science*, 2017, **4**, 1700194.
31. S. G. Kumar and L. G. Devi, *The Journal of Physical Chemistry A*, 2011, **115**, 13211-13241.
32. X. Li, Y. Sun, T. Xiong, G. Jiang, Y. Zhang, Z. Wu and F. Dong, *Journal of Catalysis*, 2017, **352**, 102-112.
33. S. M. Ghoreishian, K. S. Ranjith, H. Lee, H.-i. Ju, S. Zeinali Nikoo, Y.-K. Han and Y. S. Huh, *Journal of Hazardous Materials*, 2020, **391**, 122249.
34. S. M. Ghoreishian, K. S. Ranjith, B. Park, S.-K. Hwang, R. Hosseini, R. Behjatmanesh-Ardakani, S. M. Pourmortazavi, H. U. Lee, B. Son, S. Mirsadeghi, Y.-K. Han and Y. S. Huh, *Chemical Engineering Journal*, 2021, **419**, 129530.

35. S. M. Ghoreishian, K. S. Ranjith, M. Ghasemi, B. Park, S.-K. Hwang, N. Irannejad, M. Norouzi, S. Y. Park, R. Behjatmanesh-Ardakani, S. M. Pourmortazavi, S. Mirsadeghi, Y.-K. Han and Y. S. Huh, *Chemical Engineering Journal*, 2023, **452**, 139435.
36. K. Sridharan, S. Shenoy, S. G. Kumar, C. Terashima, A. Fujishima and S. Pitchaimuthu, *Journal*, 2021, **11**.
37. S. Chen, D. Huang, M. Cheng, L. Lei, Y. Chen, C. Zhou, R. Deng and B. Li, *Journal of Materials Chemistry A*, 2021, **9**, 196-233.
38. Y. Zhang, G. Zhang, J. Di and J. Xia, *Current Opinion in Green and Sustainable Chemistry*, 2023, **39**, 100718.
39. R. He, D. Xu, B. Cheng, J. Yu and W. Ho, *Nanoscale Horizons*, 2018, **3**, 464-504.
40. J. Z. Hassan, A. Raza, U. Qumar and G. Li, *Sustainable Materials and Technologies*, 2022, **33**, e00478.
41. S. S. M. Bhat and H. W. Jang, *ChemSusChem*, 2017, **10**, 3001-3018.
42. K. Xu, L. Wang, X. Xu, S. X. Dou, W. Hao and Y. Du, *Energy Storage Materials*, 2019, **19**, 446-463.
43. D. Chen, Z. Xie, Y. Tong and Y. Huang, *Energy & Fuels*, 2022, **36**, 9932-9949.
44. S. Wang, L. Wang and W. Huang, *Journal of Materials Chemistry A*, 2020, **8**, 24307-24352.
45. A. Kumar, P. Singh, A. A. P. Khan, Q. V. Le, V.-H. Nguyen, S. Thakur and P. Raizada, *Chemical Engineering Journal*, 2022, **439**, 135563.
46. H. Sudrajat and M. Nobatova, *RSC Applied Interfaces*, 2025, **2**, 599-619.
47. J. Low, J. Yu, M. Jaroniec, S. Wageh and A. A. Al-Ghamdi, *Advanced Materials*, 2017, **29**, 1601694.
48. P. C P, M. Srinivas and S. G. Kumar, *Inorganic Chemistry Frontiers*, 2025, **12**, 2138-2181.
49. S. G. Kumar and K. S. R. K. Rao, *RSC Advances*, 2015, **5**, 3306-3351.
50. A. Balapure, J. Ray Dutta and R. Ganesan, *RSC Applied Interfaces*, 2024, **1**, 43-69.
51. S. Harrison and M. Hayne, *Scientific Reports*, 2017, **7**, 11638.
52. W. Zhang, A. R. Mohamed and W.-J. Ong, *Angewandte Chemie International Edition*, 2020, **59**, 22894-22915.
53. A. Ghosh, A. Pramanik, S. Pal and P. Sarkar, *The Journal of Physical Chemistry Letters*, 2024, **15**, 6841-6851.
54. Q. Xu, L. Zhang, B. Cheng, J. Fan and J. Yu, *Chem*, 2020, **6**, 1543-1559.
55. R. Kavitha, C. Manjunatha, J. Yu and S. G. Kumar, *EnergyChem*, 2025, **7**, 100159.
56. L. Huang, Z. Duan, Y. Song, Q. Li and L. Chen, *ACS Applied Nano Materials*, 2021, **4**, 3576-3585.
57. T. Wei, H. Xiao, R. Niu, B. Xu, H. Li, X. Yan, Y. Li, H. Ou, B. Lin and G. Yang, *Chemical Engineering Science*, 2024, **292**, 120012.
58. K. Wang, T. Sun, H. Ma, R.-J. You, Z.-H. He, J.-G. Chen, H. Wang, W. Wang, Y. Yang, L. Wang and Z.-T. Liu, *Separation and Purification Technology*, 2024, **340**, 126786.
59. X. Li, J. Yu, M. Jaroniec and X. Chen, *Chemical Reviews*, 2019, **119**, 3962-4179.
60. M. Wang, S. Zeng, A. R. Woldu and L. Hu, *Nano Energy*, 2022, **104**, 107925.
61. A. E. Mesoudy, D. Machon, A. Ruediger, A. Jaouad, F. Alibart, S. Ecoffey and D. Drouin, *Thin Solid Films*, 2023, **769**, 139737.
62. C. Sushma and S. G. Kumar, *Inorganic Chemistry Frontiers*, 2017, **4**, 1250-1267.
63. P. Qiu, H. Liu, G. Wang, C. Wang, Z. Huang, C. Huang, Y. Lai, C. Xing and K. Liang, *Journal of Water Process Engineering*, 2024, **68**, 106372.
64. S. Liu, J. Sun, G. Ren and X. Meng, *Materials Science in Semiconductor Processing*, 2022, **137**, 106230.

65. S. G. Kumar and K. S. R. K. Rao, *Applied Surface Science*, 2017, **391**, 124-148.
66. Z. Ali, J. Ma, M. Hong and R. Sun, *Journal of Materials Chemistry A*, 2023, **11**, 3297-3314.
67. S.-S. Wang, X. Liang, Y.-K. Lv, Y.-Y. Li, R.-H. Zhou, H.-C. Yao and Z.-J. Li, *ACS Applied Energy Materials*, 2022, **5**, 1149-1158.
68. Y. Wang, E. Chen and J. Tang, *ACS Catalysis*, 2022, **12**, 7300-7316.
69. F. Wang, J. Guo, L. Han, H. Shen, L. Zhu and S. Chen, *Chemical Engineering Journal*, 2023, **478**, 147365.
70. Y. Shi, G. Zhan, H. Li, X. Wang, X. Liu, L. Shi, K. Wei, C. Ling, Z. Li, H. Wang, C. Mao, X. Liu and L. Zhang, *Advanced Materials*, 2021, **33**, 2100143.
71. Y. Wang, H. Wang, L. Guo and T. He, *Journal of Colloid and Interface Science*, 2023, **648**, 889-897.
72. S. Vinoth, W.-J. Ong and A. Pandikumar, *Coordination Chemistry Reviews*, 2022, **464**, 214541.
73. T. L. Yusuf, B. O. Orimolade, D. Masekela, K. A. Adegoke, K. D. Modibane and S. S. Makgato, *Materials Today Sustainability*, 2025, **30**, 101115.
74. X. Guan, X. Zhang, C. Zhang, R. Li, J. Liu, Y. Wang, Y. Wang, C. Fan and Z. Li, *Journal of Colloid and Interface Science*, 2023, **644**, 426-436.
75. H. Jiang, W. Wang, L. Sun, T. Kong, Z. Lu, H. Tang, L. Wang and Q. Liu, *Journal of Catalysis*, 2022, **416**, 1-10.
76. X. Zhao, Y. Xia, X. Wang, N. Wen, H. Li, X. Jiao and D. Chen, *Chemical Engineering Journal*, 2022, **449**, 137874.
77. X. Liu, H. Zhang, X. Qiu, H. Ye, Y. Xie and Y. Ling, *Applied Catalysis A: General*, 2024, **671**, 119574.
78. H. Maimaitizi, A. Abulizi, D. Talifu and Y. Tursun, *Advanced Powder Technology*, 2022, **33**, 103562.
79. W. Li, Y. Zhang, W. Ran, Y. Wang, F. Tian, F. Zhang, M. Xu, D. Zhang, N. Li and T. Yan, *Applied Catalysis B: Environment and Energy*, 2024, **351**, 123978.
80. Z. Huang, J. Wu, M. Ma, J. Wang, S. Wu, X. Hu, C. Yuan and Y. Zhou, *New Journal of Chemistry*, 2022, **46**, 16889-16898.
81. Q. Liu, C. Bai, C. Zhu, W. Guo, G. Li, S. Guo, D. Kripalani, K. Zhou and R. Chen, *Advanced Science*, 2024, **11**, 2400934.
82. Q. Chen, S. Wang, B. Miao and Q. Chen, *Journal of Colloid and Interface Science*, 2024, **663**, 1005-1018.
83. T. Xu, X. Su, Y. Zhu, S. Khan, D.-L. Chen, C. Guo, J. Ning, Y. Zhong and Y. Hu, *Journal of Colloid and Interface Science*, 2023, **629**, 1027-1038.
84. Y. Wu, M. Xu, Y. Wang, B. Hu, Y. Xie and Y. Ling, *Applied Catalysis A: General*, 2024, **677**, 119708.
85. Y. Jiang, Y. Wang, Z. Zhang, Z. Dong and J. Xu, *Inorganic Chemistry*, 2022, **61**, 10557-10566.
86. Y. Chen, F. Wang, Y. Cao, F. Zhang, Y. Zou, Z. Huang, L. Ye and Y. Zhou, *ACS Applied Energy Materials*, 2020, **3**, 4610-4618.
87. Q.-s. Wang, Y.-c. Yuan, X. Hu, D.-w. Jin, F.-k. Zhang, X.-j. Liu, J.-f. Deng, W.-g. Pan and R.-t. Guo, *Energy & Fuels*, 2024, **38**, 4554-4565.
88. A. Nawaz, S. Goudarzi, M. A. Asghari, S. Pichiah, G. S. Selopal, F. Rosei, Z. M. Wang and H. Zarrin, *ACS Applied Nano Materials*, 2021, **4**, 11323-11352.
89. Z.-w. Zhang, R.-t. Guo, J.-y. Tang, Y.-f. Miao, J.-w. Gu and W.-g. Pan, *Journal of CO2 Utilization*, 2021, **45**, 101453.
90. T. zhang, M. Maihemllti, K. Okitsu, D. Talifur, Y. Tursun and A. Abulizi, *Applied Surface Science*, 2021, **556**, 149828.

91. D. Liu, D. Chen, N. Li, Q. Xu, H. Li, J. He and J. Lu, *Angewandte Chemie International Edition*, 2020, **59**, 4519-4524.
92. Y. Xi, W. Mo, Z. Fan, L. Hu, W. Chen, Y. Zhang, P. Wang, S. Zhong, Y. Zhao and S. Bai, *Journal of Materials Chemistry A*, 2022, **10**, 20934-20945.
93. J. Ma, L. Xu, Z. Yin, Z. Li, X. Dong, Z. Song, D. Chen, R. Hu, Q. Wang, J. Han, Z. Yang, J. Qiu and Y. Li, *Applied Catalysis B: Environment and Energy*, 2024, **344**, 123601.
94. J. Wu, K. Li, S. Yang, C. Song and X. Guo, *Chemical Engineering Journal*, 2023, **452**, 139493.
95. X. Wei, M. U. Akbar, A. Raza and G. Li, *Nanoscale Advances*, 2021, **3**, 3353-3372.
96. Y. Lu, D. Wu, Y. Qin, Y. Xie, Y. Ling, H. Ye and Y. Zhang, *Separation and Purification Technology*, 2022, **302**, 122090.
97. C. Yan, M. Xu, W. Cao, Q. Chen, X. Song, P. Huo, W. Zhou and H. Wang, *Journal of Environmental Chemical Engineering*, 2023, **11**, 111479.
98. Z. Qian, L. Zhang, Y. Zhang and H. Cui, *Separation and Purification Technology*, 2023, **324**, 124581.
99. D. Qin, Y. Zhou, W. Wang, C. Zhang, G. Zeng, D. Huang, L. Wang, H. Wang, Y. Yang, L. Lei, S. Chen and D. He, *Journal of Materials Chemistry A*, 2020, **8**, 19156-19195.
100. J.-y. Zhu, Y.-p. Li, X.-j. Wang, J. Zhao, Y.-s. Wu and F.-t. Li, *ACS Sustainable Chemistry & Engineering*, 2019, **7**, 14953-14961.
101. Z. Miao, Q. Wang, Y. Zhang, L. Meng and X. Wang, *Applied Catalysis B: Environmental*, 2022, **301**, 120802.
102. H. Y. Yin, Y. F. Zheng and X. C. Song, *RSC Advances*, 2019, **9**, 11005-11012.
103. Z. Zhang, L. Li, Y. Jiang and J. Xu, *Inorganic Chemistry*, 2022, **61**, 3351-3360.
104. W. Sun, J. Liu, F. Ran, N. Li, Z. Li, Y. Li and K. Wang, *Dalton Transactions*, 2024, **53**, 14018-14027.
105. Z. Wang, B. Cheng, L. Zhang, J. Yu and H. Tan, *Solar RRL*, 2022, **6**, 2100587.
106. A. H. Bhosale, S. Narra, S. S. Bhosale and E. W.-G. Diau, *The Journal of Physical Chemistry Letters*, 2022, **13**, 7987-7993.
107. N. Sun, M. Zhou, X. Ma, Z. Cheng, J. Wu, Y. Qi, Y. Sun, F. Zhou, Y. Shen and S. Lu, *Journal of CO2 Utilization*, 2022, **65**, 102220.
108. C. Yang, Q. Zhang, W. Wang, B. Cheng, J. Yu and S. Cao, *Science China Materials*, 2024, **67**, 1830-1838.
109. T. Li, R. Tao, Y. Wang, T. Yan, X. Fan and K. Liu, *Journal of Colloid and Interface Science*, 2024, **655**, 841-851.
110. Z. Wang, B. Cheng, L. Zhang, J. Yu, Y. Li, S. Wageh and A. A. Al-Ghamdi, *Chinese Journal of Catalysis*, 2022, **43**, 1657-1666.
111. H. Fu, T. Zhang, A. Abulizi, K. Okitsu and Y. Tursun, *Optical Materials*, 2023, **139**, 113790.
112. H. Li, D. Wang, C. Miao, F. xia, Y. Wang, Y. Wang, C. Liu and G. Che, *Journal of Environmental Chemical Engineering*, 2022, **10**, 108201.
113. X. Liu, S. Gu, Y. Zhao, G. Zhou and W. Li, *Journal of Materials Science & Technology*, 2020, **56**, 45-68.
114. J. H. Kim, G. Magesh, H. J. Kang, M. Banu, J. H. Kim, J. Lee and J. S. Lee, *Nano Energy*, 2015, **15**, 153-163.
115. Q. Shi, Z. Li, L. Chen, X. Zhang, W. Han, M. Xie, J. Yang and L. Jing, *Applied Catalysis B: Environmental*, 2019, **244**, 641-649.
116. R. Kavitha and S. G. Kumar, *Chemical Papers*, 2020, **74**, 717-756.
117. R. Kavitha and S. G. Kumar, *Materials Science in Semiconductor Processing*, 2019, **93**, 59-91.

118. C. Zhou, S. Wang, Z. Zhao, Z. Shi, S. Yan and Z. Zou, *Advanced Functional Materials*, 2018, **28**, 1801214.
119. Z. Duan, X. Zhao, C. Wei and L. Chen, *Applied Catalysis A: General*, 2020, **594**, 117459.
120. Z. Zhu, C.-X. Yang, Y.-T. Hwang, Y.-C. Lin and R.-J. Wu, *Materials Research Bulletin*, 2020, **130**, 110955.
121. Z.-H. Wei, Y.-F. Wang, Y.-Y. Li, L. Zhang, H.-C. Yao and Z.-J. Li, *Journal of CO2 Utilization*, 2018, **28**, 15-25.
122. X. Yue, L. Cheng, J. Fan and Q. Xiang, *Applied Catalysis B: Environmental*, 2022, **304**, 120979.
123. X. Wang, Y. Wang, M. Gao, J. Shen, X. Pu, Z. Zhang, H. Lin and X. Wang, *Applied Catalysis B: Environmental*, 2020, **270**, 118876.
124. M. Ahmadi, S. M. Alavi and A. Larimi, *Surfaces and Interfaces*, 2024, **45**, 103908.
125. L.-X. Liu, J. Fu, L.-P. Jiang, J.-R. Zhang, W. Zhu and Y. Lin, *ACS Applied Materials & Interfaces*, 2019, **11**, 26024-26031.
126. S. Yoshino, K. Sato, Y. Yamaguchi, A. Iwase and A. Kudo, *ACS Applied Energy Materials*, 2020, **3**, 10001-10007.
127. X. Y. Kong, W. Q. Lee, A. R. Mohamed and S.-P. Chai, *Chemical Engineering Journal*, 2019, **372**, 1183-1193.
128. S. Girish Kumar and K. S. R. Koteswara Rao, *Applied Surface Science*, 2015, **355**, 939-958.
129. J. F. de Brito, C. Genovese, F. Tavella, C. Ampelli, M. V. Boldrin Zanoni, G. Centi and S. Perathoner, *ChemSusChem*, 2019, **12**, 4274-4284.
130. K. Du, G. Li, J. Yang and S. Zhang, *Powder Technology*, 2024, **439**, 119656.
131. J. Liu, T. Du, P. Chen, Q. Yue, H. Wang, L. Zhou and Y. Wang, *Applied Surface Science*, 2024, **664**, 160274.
132. A. Rana, Sonu, A. Sudhaik, A. Chawla, P. Raizada, A. K. Kaushik, T. Ahamad, S. Kaya, N. Kumar and P. Singh, *Industrial & Engineering Chemistry Research*, 2024, **63**, 6960-6973.
133. Y. Feng, D. Chen, Y. Zhong, Z. He, S. Ma, H. Ding, W. Ao, X. Wu and M. Niu, *ACS Applied Materials & Interfaces*, 2023, **15**, 9221-9230.
134. Z. Li, Z. Li, J. Liang, W. Fan, Y. Li, Y. Shen, D. Huang, Z. Yu, S. Wang and Y. Hou, *Separation and Purification Technology*, 2023, **310**, 123197.
135. L. Zhao, H. Hou, L. Wang, C. R. Bowen, J. Wang, R. Yan, X. Zhan, H. Yang, M. Yang and W. Yang, *Chemical Engineering Journal*, 2024, **480**, 148033.
136. Y. Gong, L. Shen, Z. Kang, K. Liu, Q. Du, D. Ye, H. Zhao, X. A. Sun and J. Zhang, *Journal of Materials Chemistry A*, 2020, **8**, 21408-21433.
137. G. Li, Y. Li, H. Liu, Y. Guo, Y. Li and D. Zhu, *Chemical Communications*, 2010, **46**, 3256-3258.
138. C. Yang, Y. Wang, J. Yu and S. Cao, *ACS Applied Energy Materials*, 2021, **4**, 8734-8738.
139. J. Li, Y. Zhao, M. Xia, H. An, H. Bai, J. Wei, B. Yang and G. Yang, *Applied Catalysis B: Environmental*, 2020, **261**, 118244.
140. Y. Li, J. Jiang, C. Zhu, W. Feng, S. Han and L. Li, *Journal of Environmental Sciences*, 2025, **154**, 665-677.
141. J. Li, F. Wei, Z. Xiu and X. Han, *Chemical Engineering Journal*, 2022, **446**, 137129.
142. Q. Tang, W. Tao, J. Hu, T. Gui, Z. Wang, Y. Xiao, R. Song, Y. Jiang and S. Guo, *ACS Applied Nano Materials*, 2023, **6**, 17130-17139.
143. Y. Liu, R. Zou, Z. Chen, W. Tu, R. Xia, E. I. Iwuoha and X. Peng, *ACS Catalysis*, 2024, **14**, 138-147.

144. Y.-Y. Li, J.-S. Fan, R.-Q. Tan, H.-C. Yao, Y. Peng, Q.-C. Liu and Z.-J. Li, *ACS Applied Materials & Interfaces*, 2020, **12**, 54507-54516.
145. L. Wu, S. Zheng, H. Lin, S. Zhou, A. Mahmoud Idris, J. Wang, S. Li and Z. Li, *Journal of Colloid and Interface Science*, 2023, **629**, 233-242.
146. M. Zhang, Y. Mao, X. Bao, G. Zhai, D. Xiao, D. Liu, P. Wang, H. Cheng, Y. Liu, Z. Zheng, Y. Dai, Y. Fan, Z. Wang and B. Huang, *Angewandte Chemie International Edition*, 2023, **62**, e202302919.
147. I. T. Chen, M.-W. Zheng, Y.-C. Pu and S.-H. Liu, *International Journal of Energy Research*, 2022, **46**, 15198-15210.
148. J. Su, G.-D. Li, X.-H. Li and J.-S. Chen, *Advanced Science*, 2019, **6**, 1801702.
149. H. Wei, F. Meng, H. Zhang, W. Yu, J. Li and S. Yao, *Journal of Materials Science & Technology*, 2024, **185**, 107-120.
150. J. He, J. Lin, Y. Zhang, Y. Hu, Q. Huang, G. Zhou, W. Li, J. Hu, N. Hu and Z. Yang, *Chemical Engineering Journal*, 2024, **480**, 148036.
151. W. Dai, W. Xiong, J. Yu, S. Zhang, B. Li, L. Yang, T. Wang, X. Luo, J. Zou and S. Luo, *ACS Applied Materials & Interfaces*, 2020, **12**, 25861-25874.
152. B. Yu, Y. Wu, F. Meng, Q. Wang, X. Jia, M. Wasim Khan, C. Huang, S. Zhang, L. Yang and H. Wu, *Chemical Engineering Journal*, 2022, **429**, 132456.
153. Y. Liu, X. Kong, X. Guo, Q. Li, J. Ke, R. Wang, Q. Li, Z. Geng and J. Zeng, *ACS Catalysis*, 2020, **10**, 1077-1085.
154. M. Ahmadi, S. M. Alavi and A. Larimi, *Inorganic Chemistry*, 2023, **62**, 20372-20389.
155. Y. Zhou, W. Jiao, Y. Xie, F. He, Y. Ling, Q. Yang, J. Zhao, H. Ye and Y. Hou, *Journal of Colloid and Interface Science*, 2022, **608**, 2213-2223.
156. S. Li, N. Hasan, F. Zhang, J.-S. Bae and C. Liu, *Journal of Colloid and Interface Science*, 2023, **652**, 1533-1544.
157. Y. Zhang, S. Liu, X. Guo, H. Mikulčić, R. Xiao and X. Wang, *Journal of Photochemistry and Photobiology A: Chemistry*, 2024, **447**, 115278.
158. Y. Zhu, R. Wu, J. Hui, Z. Zhang and S. Wei, *Journal of Alloys and Compounds*, 2024, **1003**, 175609.
159. X. Bai, L. He, W. Zhang, F. Lv, Y. Zheng, X. Kong, D. Wang and Y. Zhao, *Journal*, 2023, **13**.
160. M. Guo, Z. Wang, X. Wu, J. Qiu, L. Gu and Z. Yang, *ACS Applied Energy Materials*, 2023, **6**, 2863-2876.
161. Y. Wu, J. Xiao, J. Yuan, L. Wang, S. Luo, Z. Zhang, X. Fu and W. Dai, *Journal of Colloid and Interface Science*, 2024, **674**, 158-167.
162. Y. Xie, C. Qiu, L. Wang, Y. Wang, J. Zhang, J. Zhang, H. Wan and G. Guan, *Ceramics International*, 2024, **50**, 25161-25169.
163. C. Zhou, X. Shi, D. Li, Q. Song, Y. Zhou, D. Jiang and W. Shi, *Journal of Colloid and Interface Science*, 2021, **599**, 245-254.
164. X. Hu, J. Hu, Q. Peng, X. Ma, S. Dong and H. Wang, *Materials Research Bulletin*, 2020, **122**, 110682.
165. S. Song, Z. Song, H. Han, K. Wei, W. Zhang, D. Liu, Q. Wang, C. Ma, S. Feng and X. Duan, *Applied Catalysis A: General*, 2024, **683**, 119834.
166. W. Wang, X. Feng, L. Chen and F. Zhang, *Industrial & Engineering Chemistry Research*, 2021, **60**, 18384-18396.
167. M. Sun, K. Fan, C. Liu, T. Gui, C. Dai, Y. Jia, X. Liu and C. Zeng, *Langmuir*, 2024, **40**, 12681-12688.
168. X. Yu, F. Wen, F. Zhang, P. Yang, Y. Zhao, Y. Wu, Y. Wang and Z. Liu, *ChemSusChem*, 2020, **13**, 5565-5570.
169. Y. Sun, X. Qi, R. Li, Y. Xie, Q. Tang and B. Ren, *Optical Materials*, 2020, **108**, 110170.

170. H. Wang, H. Zhu, Y. Nie, X. Zhang and G. Xiang, *ACS Applied Materials & Interfaces*, 2025, **17**, 39218-39225.
171. R. Fang, Z. Yang, Z. Wang, J. He, J. Qiu, J. Ran and R. Godin, *Fuel*, 2024, **367**, 131514.
172. S. G. Kumar and K. S. R. K. Rao, *Nanoscale*, 2014, **6**, 11574-11632.
173. M. Sahu and C. Park, *Materials Today Sustainability*, 2023, **23**, 100441.
174. X. Zhao, Z. Duan and L. Chen, *Industrial & Engineering Chemistry Research*, 2019, **58**, 10402-10409.
175. X. Jia, J. Cao, H. Sun, X. Li, H. Lin and S. Chen, *Applied Catalysis B: Environmental*, 2024, **343**, 123522.
176. K. Wang, X. Feng, Y. Shangguan, X. Wu and H. Chen, *Chinese Journal of Catalysis*, 2022, **43**, 246-254.
177. S. She, B. Zhao, J. Wang, Z. Wei, X. Wu and Y. Li, *Separation and Purification Technology*, 2023, **309**, 123064.
178. H. Tang, X. Wang, C. Yao and Z. Zhang, *Separation and Purification Technology*, 2024, **338**, 126544.
179. Y. Huo, J. Zhang, Z. Wang, K. Dai, C. Pan and C. Liang, *Journal of Colloid and Interface Science*, 2021, **585**, 684-693.
180. D.-E. Lee, N. Mameda, K. P. Reddy, B. M. Abraham, W.-K. Jo and S. Tonda, *Journal of Materials Science & Technology*, 2023, **161**, 74-87.
181. P. J. Mafa, M. E. Malefane, A. O. Oladipo, S. L. Lebelo, D. Liu, J. Gui, B. B. Mamba and A. T. Kuvarega, *Journal of Environmental Chemical Engineering*, 2025, **13**, 117821.
182. S. Zhang, Y. Si, B. Li, L. Yang, W. Dai and S. Luo, *Small*, 2021, **17**, 2004980.

View Article Online
DOI: 10.1039/D5LF00154D

Data Availability

No data used in this article.